Pressure evolution during the recharge of a bubbly magma reservoir

Fakhri Bintang

Pressure evolution during the recharge of a bubbly magma reservoir

Fakhri Bintang

MScR. Volcanology

Department of Earth Sciences,

Durham University

2023

Mt. Bromo. Upon seeing this volcano as a teenager, my passion and desire to pursue magmatic studies was ignited. May this be the first major step in my ambition to contribute towards the global scientific understanding of magmatic processes.

For a 10-minute video presentation summarising the main findings of this thesis, please scan the following QR code, or follow the video link:

https://www.youtube.com/watch?v=spcuF2Qdu4s&t=15s

Table of Contents

Table of Figures

List of Tables

Abstract

Pressurization of magma reservoirs through the recharge of fresh magma is an important process in magmatic systems and has been associated with pre-eruptive ground deformation, eruption triggers and effusive/extrusive eruption styles. Long-lived shallow magma reservoirs may contain an exsolved volatile gas phase in the form of bubbles suspended in incompressible melt making the magma compressible. Bubbles could mitigate pressurization through their compressibility, and by resorbing volatiles. In this study, we use numerical models to investigate the effect of magma compressibility added by a soluble gas bubble phase, and to calculate the pressure response of a bubbly magma under a known recharge rate. I investigate this in three stages. Firstly, I use a simplified 'toy model' to understand the fundamental processes of a compressing gas-liquid system in a simple one-dimensional piston geometry. Secondly, I adapt the model to calculate the pressure evolution of a spherical bubble surrounded by an incompressible melt shell and quantify the relative contributions of the gas pressure, surface tension acting on the bubble and viscous resistance from the melt shell toward the overall magma pressure as the sum of the 3 components. Finally, I adapt the model to investigate the pressure response of a bubbly magma body under a magma injection event. To ensure consistency with the previous two scenarios, I assume the end-member scenario of rigid reservoir walls and no magma mixing, so that the change in volume must be accommodated by a reduction in the volume of the pre-existing bubbles. Across all three stages, I find that the pressure evolution of the gas is dependent on the rate at which the gas can be resorbed. The pressure evolution can be described by a dimensionless Peclet number ($Pe = \lambda_R \,/\, \lambda_D$), which captures the ratio of the compression timescale λ_R and the diffusive timescale λ_D. We first consider two end-members: 1) a no diffusive flux regime ($Pe \ll 1$) in which all the gas molecules remain in the bubble and the volume change is entirely accommodated by compression of the gas according to its equation-of-state (i.e. the gas is treated as insoluble); and 2) an equilibrium regime ($Pe \gg 1$) in which diffusion and resorption occur at perfect equilibrium with evolving pressure. Regime (1) constitutes the maximum rate of pressure increase, and regime (2) the minimum rate of pressure increase, for a given recharge rate. Furthermore, we find that the effects of surface tension and viscous resistance play a negligible role in the pressure evolution of large-scale natural magmatic systems undergoing recharge, therefore, we can reasonably assume that the gas pressure reflects the overall pressure of the magma.

However, viscosity and surface tension may be important factors for smaller systems such as laboratory experiments with high viscosity, low volume magmas. Finally, we find that, for natural estimates for bubble-bearing reservoirs under geological constraints of volume and injection rate, Pe is consistently well within the equilibrium regime ($Pe \gg 1$). The system exhibits disequilibrium behaviour ($Pe \leq 1$) only under extreme conditions, which are highly unlikely in nature. We conclude that models of pressure evolution in a recharging magma reservoir are justified in using the simpler equilibrium model, for which an implicit analytical solution is provided.

1 - Introduction

Volcanic eruptions are fed by magma, which is a mixture of silicate melt, solid crystals and under some conditions, gas bubbles. Prior to eruption, magma is stored in subsurface magma reservoirs within the crust. Magma reservoirs are periodically subject to an injection or recharge of fresh magma, this causes a magma reservoir to pressurise. Pressure evolution of a magma reservoir is extremely important as it is associated with an inflation of the magma reservoir (Mogi, 1958; Segall, 2019) and eventually, triggering a volcanic eruption if the pressure reaches a threshold value (Blake, 1981). Therefore, a good understanding of the pressure evolution of a magma reservoir is paramount for volcano monitoring to predict eruption triggers, sizes, and effects.

Crustal magma reservoirs may contain a suspension of bubbles within the magma which form due to exsolution of dissolved gasses. Bubbles play a critical role in the physical processes of a magmatic system; compressibility due to bubbles and volatile resorption could mitigate pressurization of a magma reservoir under recharge (Huppert & Woods, 2002; Le Mével et al., 2016). In this study, the effect of bubbles on the pressure evolution during the recharge of a magma reservoir is investigated.

Modern understanding of the subsurface architecture of magma storage regions beneath volcanoes holds that magma is stored in a large transcrustal “mush” complex, a 3-phase mixture of liquid melt, solid crystals and gas bubbles (Cashman *et al*.,2017; Edmonds *et al.*, 2019). Much of a transcrustal mush system is dominated by solid crystals, for example, the transcrustal mush system below Yellowstone is believed to only have < 15% bulk melt fraction (Farrell et al., 2014). Magmas are highly unlikely to erupt if the crystal fraction is >50% due to high viscosity (Marsh, 1981), so therefore, much of a mush system is immobile. However, within the mush are localised regions of melt-rich, crystal-poor magma; the lower the crystal fraction of magma, the less viscous the magma (Lesher & Spera, 2015; Roscoe, 1952). Therefore, regions of melt rich magma are the most mobile regions and are defined as “eruptible” magma bodies. For the purpose of this study, we simply define “magma reservoirs” as regions of crystal-free magma composed of silicate melt and H_2O bubbles.

Shallow magma reservoirs pressurize and inflate due to the intrusion of new magma from deeper sources (e.g., Newman et al., 2012; Degruyter et al., 2016; Delgado et al., 2016). This inflation manifests at the surface as topographic displacement above the reservoir. The Mogi model (Mogi, 1958), assuming an incompressible magma and an elastic half-space, allows for the estimation of pressure changes within the reservoir based on observed surface deformation. Understanding magma reservoir pressure is crucial for eruption forecasting, as eruptions are typically triggered when the internal magma overpressure surpasses the tensile strength of the surrounding wall rock, leading to brittle failure and the formation of conduits for magma ascent (Blake, 1981; Gudmundsson, 1988; Gudmundsson, 2012).

Magma also contains a volatile phase as evident by gas emissions and the presence of vesicles in erupted volcanic rock. Volatiles in magma (most notably H_2O, CO_2 & SO_2; Wallace *et al.*, (2015)) may exist dissolved in the melt, or as a separate free gas phase when exsolved. Shallow long-lived magma reservoirs may contain an exsolved gas phase in the form of an accumulation of bubbles. Continuous noneruptive degassing of deeply sourced sulphur rich gas indicates a permeable pathway for gasses to degas from deep in the magmatic system, periods of excess fluxes indicate that there may be periodic tapping of long-lived gasses trapped in the upper regions of magma reservoirs (Christopher *et al.*, 2015; Kilbride et al., 2016). Furthermore, inconsistencies between volume balances between a magma source reservoir feeding the growth of a new reservoir indicates that shallow magma has significant compressibility (Rivalta & Segall, 2008). If magmatic melt and crystals are considered negligibly compressible, this means that there must be a compressible gas phase within the magma. Given these observations, the architecture of a trans crustal magmatic system is strongly influenced by dissolved volatiles, with shallow magma reservoirs likely containing an exsolved gas bubble phase (Figure 1.1) (Christopher *et al.*, 2015; Cashman et al., 2017; Edmonds and Woods, 2018; Edmonds *et al.*, 2019). The compressibility due to bubbles in magma therefore has important implications in the pressure evolution of a magma reservoir because, during a magma recharge event, a compression of the gas phase would occur simultaneously with an elastic response from the chamber walls, thus complicating the relationship between an observed surface deformation and the pressure of the magma reservoir. Furthermore, volatile processes

within shallow magma reservoirs have also been linked with the effusive-explosive transitions of eruptions. The pressure dampening during magma recharge caused by bubble compressibility prevents excess overpressures to build up in the magma reservoir, this favours permeable outgassing and effusive eruptions (Degruyter et al., 2017; Parmigiani et al., 2016; Popa et al., 2019).

Throughout the past few decades, the dynamics of bubble growth have been studied using a series of numerical modelling and theoretical studies (e.g. Sparks, 1978; Prousevitch et al., 1993; Lyakhovskyet al., 1996; Blower et al., 2001). These studies have primarily focused on gaseous H_2O bubbles as arguably the most significant and the most abundant volatile species. Melt inclusion measurements have shown that silica rich magma can have bulk H_2O concentrations up to 7 wt% (including OH^-species) (Wallace et al., 2015). H_2O also strongly affects the physical properties of magma: greater dissolved H_2O depolymerizes the SiO_2 tetrahedral network which decreases the melt viscosity. This effect is more substantial for SiO_2 rich melts for which viscosity can span over many orders of magnitude due to variations in dissolved H_2O (approximately 3 orders of magnitude for rhyolites between 0-3wt% H_2O Figure 1.2) (Shaw, 1972; Hess and Dingwell, 1996; Giordano et al., 2008; Lesher and Spera, 2015). Furthermore, H_2O is the most soluble volatile in magma, making it important for the dynamics of shallow magma reservoirs which are at lower pressures. The amount of H_2O in the gas bubble phase relative to the dissolved phase is determined by the pressure-dependent solubility of H_2O. For example, as a magma rises, the pressure of the system decreases, which drives the solubility to decrease; this makes the magma “supersaturated” in volatiles which drives the volatiles to exsolve from the melt. This mechanism explains how bubbles may exist in a shallow magma reservoir. Conversely, when a magma is put under pressure, the solubility of H_2O increases, making the magma “undersaturated” and driving H_2O to resorb back into the melt. The latter case of a bubbly magma being subject to compression has not been studied as much as bubble growth and may have a significant effect in dampening the pressure evolution of a bubbly magma reservoir under recharge; gas resorption would reduce the number of gas molecules in the bubble, reducing the gas pressure and consequently dampening the pressure evolution of a magma reservoir.

Bubble growth is undoubtedly an extremely important process to understand for magmatic systems. Bubble growth as magma rises and decompresses plays a critical role in the mobility of magma as bubbles increase the buoyancy of magma (Anderson, 1995) and the rate of bubble growth is an important control on determining the explosivity of an eruption as rapid growth and bubble overpressure may cause magma to fragment (McBirney & Murase, 1970; Sparks, 1978; Verhoogen, 1951). This has led to bubble growth processes to be studied in great detail, and mathematical models of the process have been developed (e.g. Sparks, 1978; Prousevitch et al., 1993; Lyakhovsky et al., 1996; Blower et al., 2001; Coumans *et al.*, 2020). However, the dynamics of bubbly magma under compression is less well understood. In this study, I adapt an existing numerical model to investigate the dynamics of bubbly magma under compression.

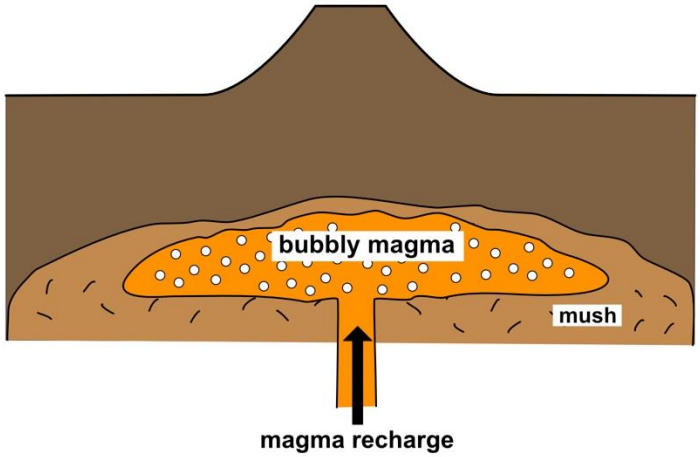

Figure 1.1 Idealised illustration of the architecture of a subsurface shallow magmatic system and the roles of exsolved volatiles within the system. This illustration focusses on the shallowest magma reservoir containing an accumulation of exsolved bubbles. The magma recharge portrays an active magma recharge from a deep conduit, but magma recharge may occur passively by percolation from the mush. Figure adapted from Edmonds et al. (2019)

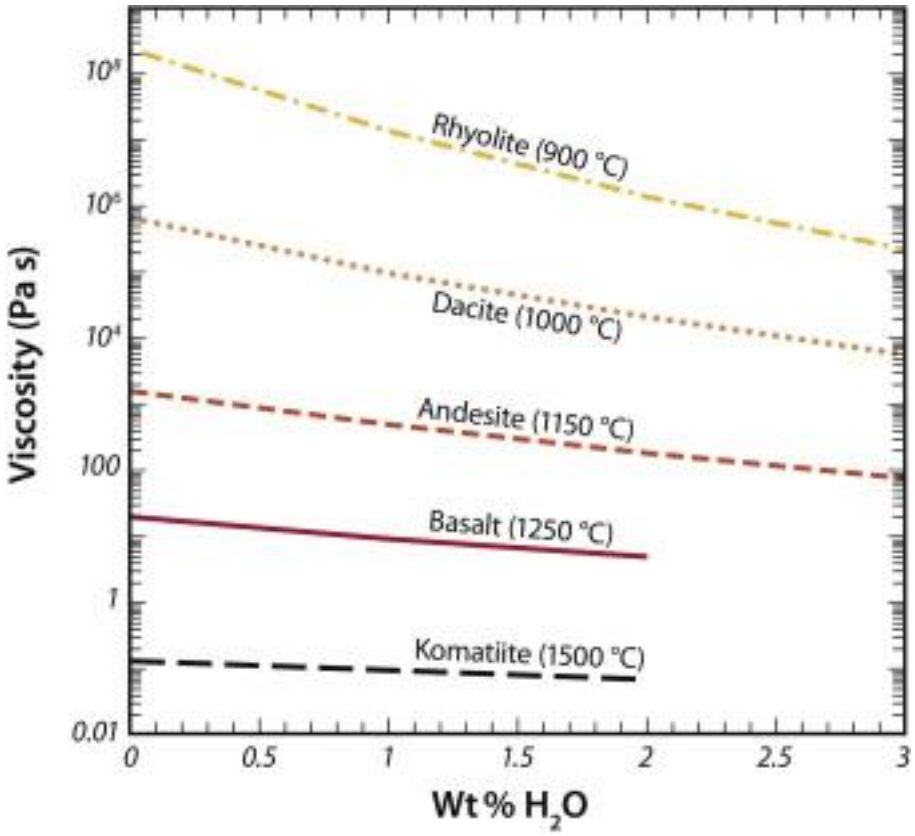

Figure 1.2. Melt viscosities due to dissolved H_2O concentration over various melt compositions and temperatures. Melt compositions of increasing silica content have a higher viscosity and lower typical eruption temperature Figure from Lesher and Spera (2015*), viscosity models to calculate the profiles from* Shaw, 1972 & Giordano, Russell and Dingwell, 2008.

1.1 Aims, motivations and methods

This study aims to better understand the physical processes that occur in bubbly magma reservoirs during a magma recharge. Figure 1.3 illustrates 2 conceptual models of a magma chamber under a recharge event. Figure 1.3a shows a magma reservoir with no bubbles subject to an injection of fresh magma, in this scenario magma is essentially incompressible so all the volume is accommodated by an elastic response from the surrounding wall rock/mush; the pressure evolution of the magma reservoir is therefore simply inferred from the observed deformation of the surface overlying the magma reservoir (Mogi, 1958). Figure 1.3b on the other hand conceptualises what would occur when bubbles are present in the magma reservoir. The bubbles make the magma effectively compressible, an elastic response from the wall rock would occur simultaneously with the compression of the bubbles as the magma reservoir pressurises. However, due to the compressibility of the bubbles and the dynamic solubility of H_2O causing the gas to resorb, the pressure evolution is dampened by the bubbles. Therefore, the pressure evolution of the magma reservoir inferred from deformation at the surface is not only due to the elastic response from the wall rock, but also due to the compressibility of the bubble phase.

Existing numerical models for the dynamics of diffusive bubble growth can output the changes in a bubbly magma volume due to an input disequilibrium (e.g. changes in pressure, temperature and supersaturation). Differences between the dissolved H_2O concentration and thermodynamic equilibrium solubility drive the exsolution/resorption of H_2O between the melt and bubble in order to reach equilibrium. The molar flux of H_2O between the melt and gas phase controls the growth rate of the bubbles and is limited by the diffusivity of H_2O across the melt. These models have been developed in a series of iterations (e.g. Sparks, 1978; Prousevitch et al., 1993; Lyakhovskyet al., 1996; Blower et al., 2001) adding additional complexity through each iteration. The latest iteration of this model by Coumans *et al.* (2020) provides an experimentally validated model and a user-friendly interface coded in MATLAB to investigate bubble growth under a range of input parameters. I adapt the model to simulate the magma pressure due to an input known volumetric compression. If we strip the elastic response from the reservoir walls in figure 1.3b for simplicity, so that injected volume is purely accommodated by a compression of the gas phase, we can use the existing

numerical model framework to isolate and investigate the effect of compressibility introduced by the bubble phase in magma and output the pressure evolution of the magma.

Two analytical end-member scenarios can describe the maximum and minimum pressure evolution of a compressing bubbly magma. 1) If we ignore the solubility of H_2O such that all the initial moles of gas stay in the bubble throughout compression, this describes the maximum pressure evolution of a bubbly magma. 2) If we consider gas resorption to occur instantaneously at equilibrium with solubility, this describes the minimum pressure evolution of the system as gasses can freely resorb back into the melt, reducing the pressure. The assumption that resorption occurs at equilibrium with solubility has been adopted in other studies that have considered the compressibility factor introduced by a bubble phase in magma (e.g. Huppert and Woods, 2002; Le Mével et al., 2016). These assumptions however, do not consider disequilibrium processes at the bubble scale. To do this, we require a numerical solution that accounts for mixed behaviour between the 2 end-member scenarios. Molecular flux rate between the volatiles in the gas and dissolved in melt phases is a strong control on the evolution of the bubble volume and is dependent on the solubility at the bubble-melt interface and the diffusivity (Prousevitch et al., 1993; Proussevitch and Sahagian, 1998). In the case of bubble growth, slow depressurisation of a bubble causes the bubbles to grow at equilibrium with solubility as the diffusion and exsolution of volatiles occurs fast enough to keep up with the decompression. However, rapid decompression of magma may introduce disequilibrium as volatile exsolution and diffusion cannot keep up with the decompression (Lyakhovsky et al., 1996).

A similar disequilibrium process may also occur during the compression of a bubbly magma; a sufficiently fast magma recharge rate into a long-lived bubbly magma body may cause the gas phase to volumetrically compress faster than resorption of gas can occur, this would leave more gas molecules trapped in the bubbles, increasing the bubble pressure in disequilibrium with the solubility. Such a scenario requires a full numerical solution that accounts for diffusivity of volatiles across the melt in order to simulate the pressure evolution, whereby the numerical model by Coumans *et al.* (2020) can solve. A numerical solver however, requires significantly more computing resources than an analytical solution. In the case that the recharge of bubbly magma is sufficiently slow enough for pressurisation

to occur at equilibrium with solubility, an analytical solution should be favoured to significantly reduce the computational resources compared to the full numerical solution.

This thesis is structured into 3 sections. Firstly, I produce a numerical model of a simplified magmatic system to isolate the diffusive controls on a compressing gas-solvent liquid system. Here, I model a closed-system cylinder containing two distinct layers of gaseous H_2O and a dissolved H_2O bearing melt respectively. I use this simple one-dimensional approach to model the volatile concentration profile across the melt and the pressure evolution of the gas, eliminating the geometric complications that arise from spherical bubbles. This aims to capture the conditions required for gas resorption to occur at varying degrees of disequilibrium by varying the timescales of diffusion and compression.
Secondly, I introduce a spherical bubble geometry to more closely resemble a bubble suspended in melt. Here I test the effects of viscous resistance from the melt and the effects of surface tension of the bubble. The relative contributions of gas pressure, viscous resistance and surface tension are assessed to determine which are the most important factors in calculating magma pressure.
Finally, the model is set up to resemble an idealised bubbly magma reservoir under recharge. The chamber walls are perfectly rigid so that the effect of volumetric compression of the bubble phase is isolated, eliminating complications arising from the elastic response from the wall rock. All three models will test parameters over the interval expected in nature, and beyond, in order to test the theoretical limits of the model.

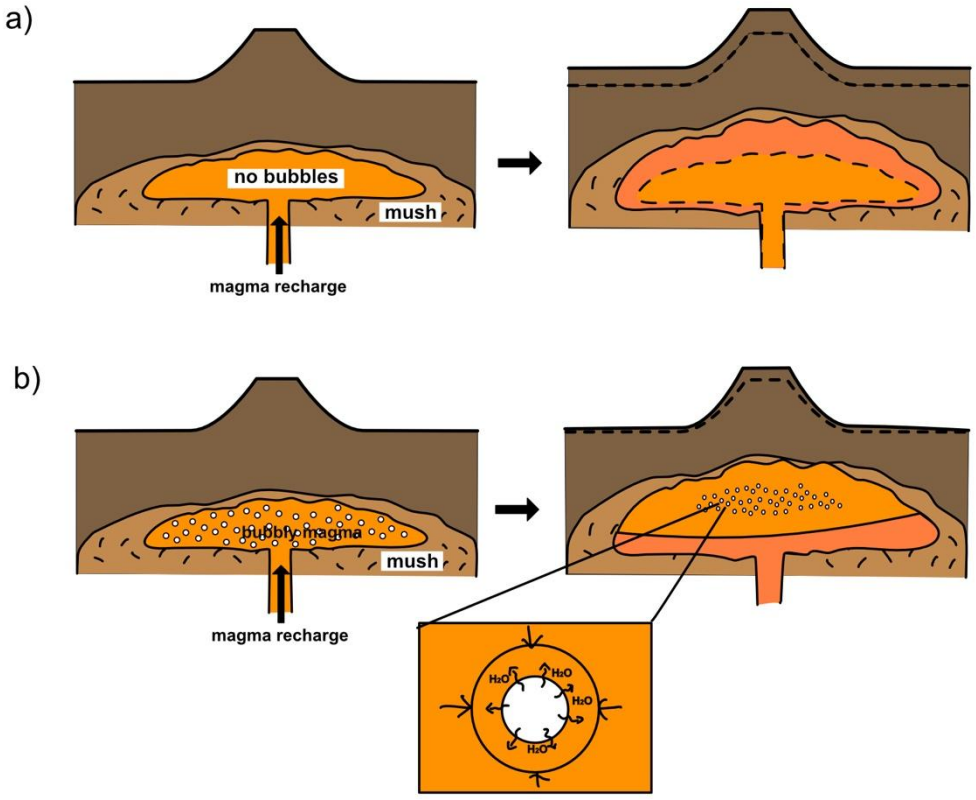

Figure 1.3. Two idealised scenarios of magma reservoirs under recharge. A) a magma reservoir with no bubbles, melt is incompressible, so the recharged volume is accommodated by an elastic response from the reservoir walls, which is directly linked to the pressure increase. B) a bubbly magma reservoir under compression. The magma is compressible, so compression of the gas phase and subsequent H_2O resorption occur simultaneously with an elastic response from the cavity walls.

2 - Gas pressure evolution in a closed soluble gas-liquid system

Compressibility is a term used to describe a material's volumetric response to an applied pressure. In magma, the solid crystals and liquid melt phases are considered negligibly compressible (compressibility values on the order of 10^{-11} Pa^{-1} (Gerya, 2019)) and therefore assumed incompressible for modelling purposes. However, gas bubbles in magma are significantly compressible, which is particularly important in shallow long-lived magma reservoirs where there is thought to be a significant gas bubble phase suspended in the melt (Edmonds et al., 2019b). The relationship between the volume and pressure evolution of a closed gas system can be defined by the ideal gas law:

$$P_g = \frac{8.314 n_g T}{V_g}, \qquad \text{(Eq. 2.1)}$$

where P_g is the gas pressure (Pa), n_g is the number of moles of gas, T is the temperature (K), V_g is the gas volume (m^3) and 8.314 is the ideal gas constant ($Jmol^{-1}K^{-1}$). Bubbly magma may compress due to a recharge of new magma where the bubbles are the dominant source of compressibility. In the simplest case where all the gas remains in the bubble and the system is isothermal, P_g evolves directly as an inverse function of V_g. However, the pressure dependent solubility of volatiles, most significantly H_2O in shallow systems, plays a crucial role because an increase in pressure causes an increase in solubility, hence gasses resorb back into the melt. During compression the gas pressure is dependent on both the gas volume (V_g) and the number of moles of H_2O in the bubble (n_g). The number of moles of gas depends, in turn, on volatile solubility and the diffusivity across the melt. Volatile diffusivity describes how easily volatiles can move through the melt by diffusion; the easier and faster volatiles can diffuse through melt, the more efficiently volatiles can be resorbed back into the melt which aids in reducing the pressure of the gas. However, it may be possible that, when the rate of volumetric gas compression is sufficiently fast compared with the rate of volatile diffusion through the melt, the rate of gas resorption may be limited by diffusion, which drives the gas pressure to increase at a faster rate as more molecules remain in the gas phase.

In this chapter I investigate the fundamental processes of closed soluble gas-liquid systems and quantify the effects of solubility and diffusivity in the calculation of P_g with a known volume change. The conditions required for the gas pressure to evolve in disequilibrium due to diffusion-limited resorption will also be investigated. This section is treated as a simplified pilot study which strips the complexities of natural magma. The insights from this study will act as a foundation upon which the following chapters will build.

2.1 Model setup

2.2 The simplified cylindrical model

We create a simple numerical 'experiment' in which a perfectly rigid, isothermal, closed-system cylinder is composed of 2 distinct layers: a compressible ideal gas; and an incompressible fluid. These represent the gas and liquid phases of magma respectively. We output the evolving pressure of the gas phase $P_g(t)$ due to a constant input compression rate dV/dt . The liquid, which has constant volume (V_L), acts as a 'piston arm' that will volumetrically compress the gas volume (V_g, V_{g0}) where pressure will be calculated by the ideal gas law at each time. The model is illustrated in figure 2.1.

For each experiment, a constant compression rate is applied to the cylinder which compresses the gas pocket and is directly proportional to the length compression rate (dR/dt) due to a constant cross-sectional area (A). Here the ideal gas law is repeated (Eq. 2.1) and written in a form to show that the gas pressure at any time is calculated as a function of the number of gas molecules at time $\big(n(t)\big)$ and the gas volume at time $(Vg(t))$:

$$P_g(t) = \frac{n(t)8.314T}{V_g(t)}, \qquad \text{(Eq. 2.1)}$$

where:

$$V_g(t) = V_{g0} + t\frac{dV}{dt}.$$

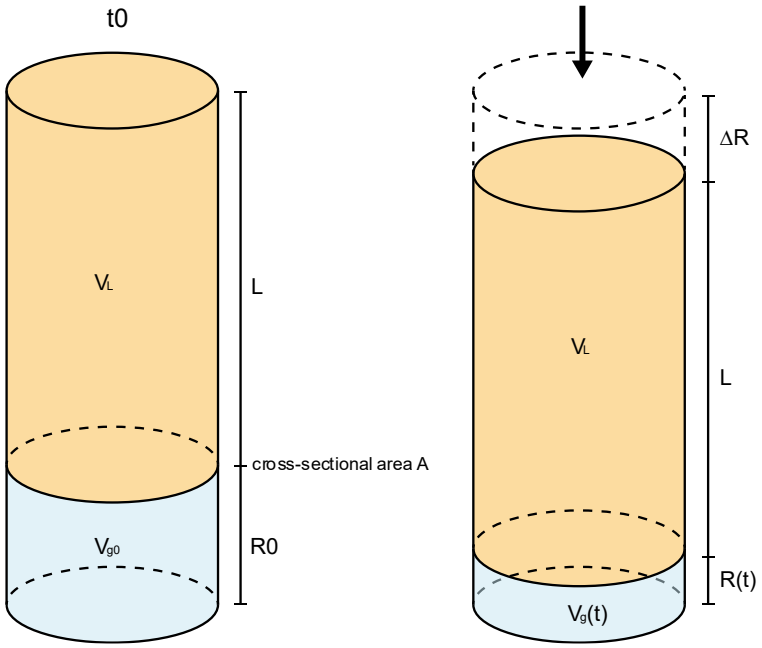

Figure 2.1. illustrating the cylindrical numerical experiment from the initial dimensions shown in the left and after a given time (t) on the right. The volume, length, and cross-sectional area of the liquid (V_L, L, A respectively) do not change. The gas volume can be calculated at each time where $V_g(t) = V_{g0} - A \cdot \Delta R(t)$. The gas fraction ϕ is calculated as $\phi = V_g/(V_g + V_L)$.

The model assumes a perfectly isothermal system so the temperature (T) remains constant throughout. This model will ignore the pressure required to move the solvent liquid piston arm and so will not account for viscous resistance of the liquid, frictional forces, or surface tension pressures; the effects of other forces acting in the case of spherical bubbles will be investigated in following chapters.

Using P_g, pressure dependent H_2O solubility concentration C_s [wt %] in rhyolitic melts can be calculated for a known temperature (Liu et al., 2005):

$$C_s = \frac{\left(354.94{P_g}^{0.5} + 9.623P_g - 1.5223{P_g}^{1.5}\right)}{T} + 0.0012439{P_g}^{1.5}. \qquad \text{(Eq. 2.2)}$$

We also start the model with P_g (in MPa) and C_s in equilibrium such that $C_0 = f(P_0, T)$. Below, are three solutions to calculating the pressure evolution of the system. These are 2 analytical end-member solutions which reflect the maximum and minimum pressure evolution of the system respectively: 1) no diffusion or resorption occurs, all the H_2O molecules remain in their initial phases throughout compression, and 2) diffusion and resorption of H_2O occur at equilibrium with the pressure dependent solubility. Finally, a full

numerical solution where the rate of H_2O resorption is controlled/limited by the diffusivity across the melt, which is the closest of the 3 solutions to reflecting a natural compressing gas-liquid system. Comparing the output pressure of the 3 solutions will determine the threshold for when gas pressure evolution is limited by diffusion of H_2O across the melt.

2.2.1 End-member solution 1 – no diffusion/no molar flux (analytical)

In the simplest solution, H_2O is considered insoluble in the melt so there is no molecular flux of H_2O between the gas and melt phases. Therefore, P_g is simply calculated as compression of an ideal gas where $n(t)$ is constant (Eq. 2.1). This reflects the maximum possible P_g evolution given any set of initial parameters as all the initial gas molecules remain in the gas throughout compression. The Pressure evolution of this solution will always tend to infinity as the bubble volume tends to zero.

2.2.2 End-member solution 2 – Equilibrium diffusion (implicit analytical)

Another possible scenario is that the gas pressure evolves at equilibrium with the solubility term (Eq. 2.2). This solution assumes that H_2O resorption and diffusion across the melt occurs instantaneously (equivalent to letting $D \rightarrow \infty$). An implicit function of the ideal gas law can be used to calculate $P_g(t)$ as solubility C_s is dependent on P_g. Combining equations 2.2 and 2.3 yields the implicit function:

$$P_g = \frac{8.314 n_g(P_g) T}{V_g}, \qquad \text{(Eq. 2.3a)}$$

where:

$$n_g(P_g) = n_{g0} + \Delta n_g = n_{g0} - \frac{[C_S(P_g) - C_0]}{100} \frac{\rho_m V_m}{18.015}. \qquad \text{(Eq. 2.3b)}$$

Solubility C_S is calculated using equation 2.3 and C_0 is the initial dissolved H_2O concentration, the units in wt% are divided by 100 to convert to weight fraction. Molar flux Δn_g is negative to represent mass removed from the bubble. Equation 2.4b describes the amount of exsolved H_2O in the system dependent on its wt% (C) relative to the melt mass. Equations 2.4 a and b contain the implicit term $n_g(P_g)$ and $C_S(P_g)$ which can be calculated by finding the roots of equation 2.4 a and b. This is numerically calculated on MATLAB using

the ‘fzero’ function at each timestep which will output the time dependent pressure vector (appendix A). The equilibrium solution represents the minimum possible gas pressure as the molar flux and concentration gradients equilibrate instantaneously with an applied disequilibrium.

2.2.3 Solution 3 – full numerical solution

This solution will most closely resemble natural processes that occur in magma. Fick’s second law of diffusivity describes the movement of the solute gas across a diffusive medium based on the spatial derivatives of the solute concentration. In magmas and in this model, H_2O is resorbed at the gas-melt interface and diffuses towards the opposite end of the melt length L. Fick’s second law can predict the evolution of the concentration profile over time. Due to the cylindrical shape of the experiment, we can assume that there is no variation on H_2O concentration across any cross-sectional slice of the melt, so all the concentration gradients occur along the melt length L. Therefore, simple 1-D modelling of diffusion can be used along the melt profile L over time using the simplest form of Fick’s second law:

$$\frac{\partial C}{\partial t} = \frac{\partial}{\partial x}\left(D\frac{\partial C}{\partial x}\right), \qquad \text{(Eq. 2.4)}$$

where C is the local H_2O concentration in wt% at a given point in the vector x of the melt length L, and D is the diffusion coefficient in m^2/s. Diffusivity in rhyolite melts can be calculated as a function of temperature, H_2O concentration and pressure at any point in time (Zhang & Ni, 2010):

$$D_{(H_2O)} = C\,exp\left(-18.10 + 1888P_g - \frac{9699+3626000P_g}{T}\right), \qquad \text{(Eq. 2.5)}$$

where T is the temperature in K and P_g is in units of MPa. For this simplified geometry, we assume a constant value for D in space and time, in order to simplify the analysis (see equation 2.10).

Forward modelling of equation 2.5 is calculated using MATLAB's built-in ordinary differential equation solver ODE15s which will also automatically calculate appropriate time-steps and resolve non-linear interations for the model towards appropriate residual tolerances (absolute = 10^{-6}, relative 10^{-4}). The model pseudo-code is available in the appendix. A boundary condition at each timestep is assigned as the solubility from the previous timestep's gas pressure calculated from equations 2.4 & 2.5 at the gas-melt interface ($x = 0$). Equation 2.5 is calculated by the concentration gradients across the melt length created by the boundary condition. The H_2O concentration flux ($\partial C/\partial t$) is taken as an output of the model so the concentration profile evolution of the melt shell can be plotted. The molar flux (Δn) of H_2O between the gas and the melt at each timestep can be calculated numerically by finding the difference between the initial concentration profile and the trapezoidal integral of the dissolved H_2O profile in the melt at each time t:

$$\Delta n = \frac{A\rho_m}{18.015}\frac{1}{100}\left(\int_0^L C_0 dx - \int_0^L C(t)dx\right), \qquad \text{(Eq. 2.6)}$$

where A is the surface area of the melt-gas interface in m^2, ρ_m is the melt density in kg/m^3 and C_0 is the initial melt concentration in wt%. The limits for intergration are taken across the melt layer from zero to the total melt length L. Molar flux Δn is then fed into equation 2.4b to calculate the gas pressure at time t. For this solution, D will be considered spatially and temporally constant throughout each experiment for simplicity.

2.3 Illustrative example

I first test the model with setup parameters that roughly reflect natural shallow magma conditions (Table 2.1), this is to illustrate a dimensional example of the model processes before dimensionless analysis is applied. The initial gas and melt volumes start at 1 and 10 μm^3 respectively which represents a small bubble in magma. The gas volume fraction (ϕ) represents the fraction of the total volume made up by the gas calculated as

$$\phi = \frac{V_g}{V_g + V_m}. \qquad \text{(Eq. 2.7)}$$

Due to the melt and gas volumes being proportional to cylindrical cross-sectional area A, porosity can be derived as a relationship between R_0 and L:

$$\phi = \frac{AR_0}{A(R_0+L)} = \frac{R_0}{R_0+L}. \quad \text{(Eq. 2.8)}$$

With a cross sectional area in the gas-melt interface of 1μm^2, melt and initial gas thickness (L & R_0) are 1 and 10 μm respectively. The gas volume and concentration start at equilibrium with the initial gas pressure 50MPa and temperature of 900°C which are values chosen to reflect magma chamber pressure and temperatures. The H_2O diffusivity is calculated based on the initial solubility concentration from equation 2.3 and with a metaluminous rhyolite composition and rounded to the nearest order of magnitude. The simulations are set to end when R reaches a critical minimum value of 0.001μm, for numerical stability.

During the compression of the gas, we define two characteristic timescales. The advective or compression timescale (λ_R) is the time taken for the initial gas volume to completely compress under a constant compression rate. Due to the cylindrical dimensions of the model, the change in volume is proportional to the change in length R so we can represent the compression timescale in terms of the initial gas length (R_0) and length compression rate ($\dot{R} = dR/dt$):

$$\lambda_R = \frac{R_0}{\dot{R}} \quad \text{(Eq. 2.9)}$$

The diffusive timescale (λ_D) is the characteristic timescale for H_2O to diffuse through the melt length:

$$\lambda_D = \frac{L^2}{D}, \quad \text{(Eq. 2.10)}$$

where D is the diffusivity of H_2O in the melt (m^2s^{-1}). The ratio of the diffusive and advective timescales can describe the pressure evolution regime of the system as a dimensionless Peclet number:

$$Pe = \frac{\lambda_R}{\lambda_D} = \frac{R_0 D}{\dot{R} L^2} \quad \text{(Eq. 2.11)}$$

A high Peclet number ($Pe \gg 1$) would be associated with a short diffusive timescale (i.e., a fast diffusion rate) compared to a long advection timescale (i.e., a slow advection rate) ($\lambda_R \gg \lambda_D$). Under these conditions, we can expect that diffusion and resorption occur quickly, so that the pressure evolves at equilibrium with the solubility, making the P_g evolution match the equilibrium solution (solution 2). For the opposite case of a low Peclet number ($Pe \ll 1$), where the diffusive timescale is much longer than the advective timescale ($\lambda_R \ll \lambda_D$) ,the rate of resorption and diffusion is slower than advection so more H_2O molecules remain in the exsolved gas phase, increasing P_g away from the equilibrium solution and closer to the no diffusive flux solution (solution 1).

I test for three different compression rates that give three contrasting Peclet regimes: $Pe =$ 10^{-3}, 1 and 10^3 which correspond, respectively, to the cases where diffusion is sluggish/slow compared to advection, where the diffusive & advective timescales are equal, and where diffusion occurs much faster than advection.

Table 2.1 – Parameters used to simulate the pressure, volume and dissolved H_2O concentration evolution for the analytical end-member solutions (1 - No diffusive flux, 2 – equilibrium diffusion) and the full numerical solution (3). Parameters are roughly calibrated to natural conditions found in shallow magma reservoirs.

P_{g0}	50 MPa
T	1173.15 K
A	1 µm^2
R_0	1 µm
L	10 µm
P_m	2500 Kg/m^3
Pe	10^{-3}, 1, 10^3
C_0	2.53 wt% (Eq. 2.2)
D	1E-11 m^2/s, (Eq. 2.5 rounded)
$\dot{R}$ *(dR/dt)*	10, 0.1, 0.0001 µm/s (Eq. 2.11, based on Pe)

Figure 2.2 plots the gas pressure evolution of the three solutions for the parameters set in table 2.1 In each plot, the equilibrium solution, the no diffusive flux solution, and the full numerical solution are shown. The pressure plots for the equilibrium and no diffusive flux solutions (solutions 1 & 2) appear to have the same pressure evolution across the 3 Pe numbers but stretched in the x direction based on the λ_R of the respective Pe value of the systems. These plots confirm that the pressure evolution of the full numerical solution (solution 3) for high Pe numbers ($Pe \gg 1$) yield the same results as the equilibrium solution (solution 2) (Figure 2.2c) as hypothesised. Also, the full numerical solution pressure evolution for low Pe ($Pe \ll 1$) is very close to the no diffusive flux solution (solution 1) (Figure 2.2a). When $Pe = 1$, the solution 3 pressure remains close to the solution 2 curve but deviates upwards, particularly near the end of the simulation time, indicating a transitional regime where there are some excess H_2O molecules remaining undissolved in the gas phase.

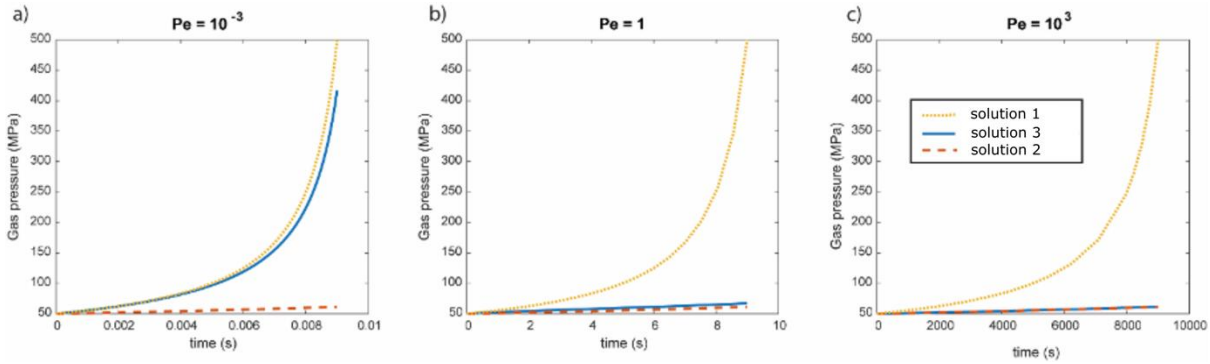

Figure 2.2. Results for the 3 simulations from table 1 outputting P_g. Solid blue lines represent the Pressure results from solution 1, dashed red lines are the results from solution 2 and the dotted yellow lines represent solution 3. (a), (b) & (c) show results for Pe<<1, Pe = 1 & Pe>>1 respectively.

2.4 Analysis methods

Pressure and time are made dimensionless to facilitate comparison of results for different parameters, and between the 3 solutions. Pressure is normalised to compare the evolution of numerical solution (3) to the end-member solutions 1 & 2:

$$\bar{P} = \frac{P_g(3) - P_g(2)}{P_g(1) - P_g(2)}, \quad \text{(Eq. 2.12)}$$

where the numbers in the brackets represents the pressure vectors calculated from solutions 1-3 respectively. The vector $\bar{P}$ shows the evolution of the pressure regime that the full numerical solution $P_g(3)$ follows over time. At $t = 0$, all simulations start as undefined as all the solutions start at the initial pressure P_0, so values are only taken from the second time-step. At early time-steps all solutions start close to $\bar{P} = 1$ as all the solutions initiate with pressures at equilibrium with solubility. After which, the normalised pressure $(\bar{P})$ evolves between 0 and 1 where $\bar{P} = 1$ indicates the pressure evolution follows the maximum pressure solution 1, and $\bar{P} = 0$ indicates that the pressure evolution follows the minimum pressure solution 2.

Two methods for normalising time can be obtained based on λ_D & λ_R (equations 2.10 & 2.11):

$$\bar{t}_R = \frac{t}{\lambda_R} = \frac{t\dot{R}}{R_0}, \quad \text{(Eq. 2.13)}$$

$$\bar{t}_D = \frac{t}{\lambda_D} = \frac{tL^2}{D}. \quad \text{(Eq. 2.14)}$$

The normalised advective time $\bar{t}_R$ is used for dimensionless analysis of $\bar{P}$ over the course of bubble compression where $\bar{t}_R$ ranges from 0 $(t = 0)$ to 1 (i.e., the time when $R = 0$). The normalised diffusive time $\bar{t}_D$ is used to show the evolution of $\bar{P}$ in terms of the diffusion timescale where there is no upper limit for $\bar{t}_D$.We expect that when $\bar{t}_D$ exceeds 1, $\bar{P}$ would be at or close to 0 as t exceeds λ_D, as H_2O has had sufficient time to resorb appreciably. Plotting any given output or normalised output against $\bar{t}_R$ reflects the evolution through the simulation time whereas plotting against $\bar{t}_D$ is a timescale based on the diffusive processes. Both timescales are useful to be plotted against for analysis.

Figure 2.3 shows a consolidated version of figures 2.2 where the evolution of gas pressure relative to the initial pressure $(P_g - P_0)$ over the normalised advective time $\bar{t}_R$, comparing the numerical solutions at different Pe regimes to the end-member solutions specified in table 1. The end-member solutions act as the maximum and minimum pressure evolution of the initial volume set in table 2.1 across any compression rate. Figure 2.2 & 2.3 also show

that when the system has $Pe > 1$, there is only a small gas pressure increase from P_0 for the bubble to completely compress and fully resorb H_2O $(\sim 10 - 20\ MPa)$. This is a very small pressure increase compared to the >450MPa P_g increase shown on the no diffusive flux pressure curves.

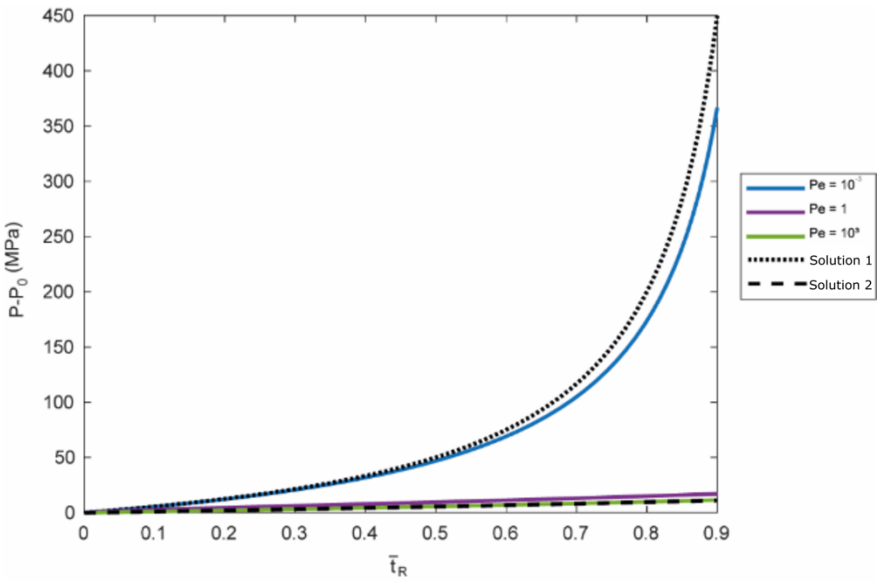

Figure 2.3. The evolution of the gas pressure increases from the initial pressure $(P_g - P_0)$ on the y axis plotted against normalised advective time $(\bar{t}_R)$ on the x axis for parameters set in table 2.1. The black lines represent the no-diffusion (solution 1, close dotted line) and equilibrium (solution 2, wider gapped dashed lines) end-member solutions. Coloured blue, purple and green lines are the evolution for the numerical solutions with compression rates corresponding to Pe = 10^{-3}, 1 & 10^3 respectively. The plot has been truncated up to $\bar{t}_R$ = 0.9, as the low Pe solution (blue line) trends to infinity at late stage t_R.

Figure 2.4a, b & c show the evolution of the *H_2O* concentration profiles along L over time for the parameters given in table 2.1. Initially, all 3 plots show the same uniform concentration profile. The lowest Pe simulation (Figure 2.4a) shows limited H_2O diffusion and resorption where the rate of diffusion is much slower than compression, H_2O does not fully diffuse to the far end of the melt x_L (the opposite end to the gas-melt interface) where the concentration at x_L remains at C_0. In this case, fewer H_2O molecules are resorbed into the melt, so the P_g evolution increases faster than the equilibrium solution. When $Pe = 1$, the melt profiles show that H_2O diffusion is incomplete. Some H_2O diffuses all the way to x_L but at lower concentrations than that of the bubble wall (Figure 2.4b). More H_2O has been resorbed into the melt than at Pe = 10^{-3} which reduces the P_g evolution closer to the

equilibrium solution. Resorption and diffusion of H_2O however, is not in equilibrium because considerable time is required for H_2O to diffuse towards x_L, therefore the P_g evolution does not match the equilibrium solution as more moles are still remaining in the gas. The highest Pe simulation shows that the H_2O concentration across the melt shows a uniform profile between x_0 and x_L at all times and increases the concentration by the equilibrium solution over time (Figure 2.4c).

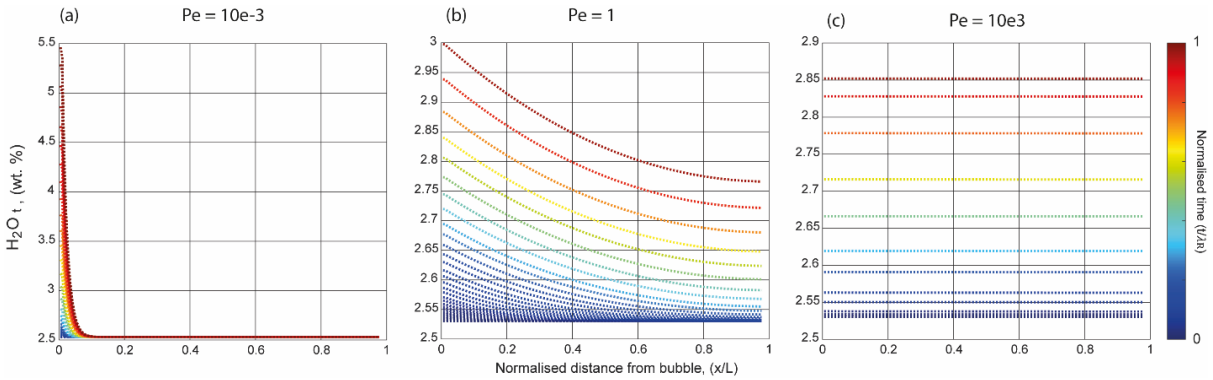

Figure 2.4.Dissolvesd H_2O concentration profiles over time Results for the 3 simulations using parameters from table 2.1. Time is normalised as t/λ_R, each profile is colour-matched to a time in the simulation. (a), (b) & (c) show results for Pe<<1, Pe = 1 & Pe>>1 respectively.

Figure 2.5 plots the normalised pressure (Eq. 2.13) against the normalised advective and diffusive times equations 2.14 & 2.15). This shows more clearly how the full numerical solution (solution 3) compares with solutions 1 and 2 over time. At $t = 0$, $\bar{P}$ is considered undefined as the calculation for $\bar{P}$ *at* $t = 0$ divides by a zero denominator (Eq. 2.13) since the pressure for all three solutions is equal to P_0. The normalised pressure starts at $\bar{P}$=1 as the models as all 3 solutions begin at the same initial pressure. The value of $\bar{P}$ begins to lower as diffusion occurs (Figure 2.5). The advective timescales show that the equilibrium solution is reached quickly when Pe*>>1* as $\bar{P}$ rapidly decays, showing a sigmoidal curve profile (Figure 2.5a), it appears that when Pe decreases towards 1, the sigmoidal curve shifts to the right showing that complete diffusion does still occur but at a slower rate. For Pe numbers *≥ 1,* $\bar{P}$ ends at zero as the pressure of solution 3 trends to infinity. When Pe*<<1,* $\bar{P}$ stays close to 1 throughout most of the simulation duration and $\bar{P}$ at $\bar{t}_R(end)$ does not reach zero indicating that the pressure closely follows solution 1 and by the end of the experiment there is a significant number of H_2O molecules undissolved in the gas (Figure

2.5a). A physical description of this is when the solution breaks down as P_g tends to infinity when the gas bubble volume gets smaller.

The diffusive timescales have the same normalised pressures as the advective timescale but under a new normalised time. The curve representing $\log_{10} Pe = 3$ shows a sigmoidal curve which represents the profile for complete equilibrium diffusion (Figure 2.5b). When $\bar{t}_D$ exceeds 1, the normalised pressure drops close to zero. The curves representing $Pe \leq 0$ fall off the high Pe curve due to the solubility increasing towards infinity due to a dramatic pressure increase which resorbs more H_2O molecules by the gas-melt interface.

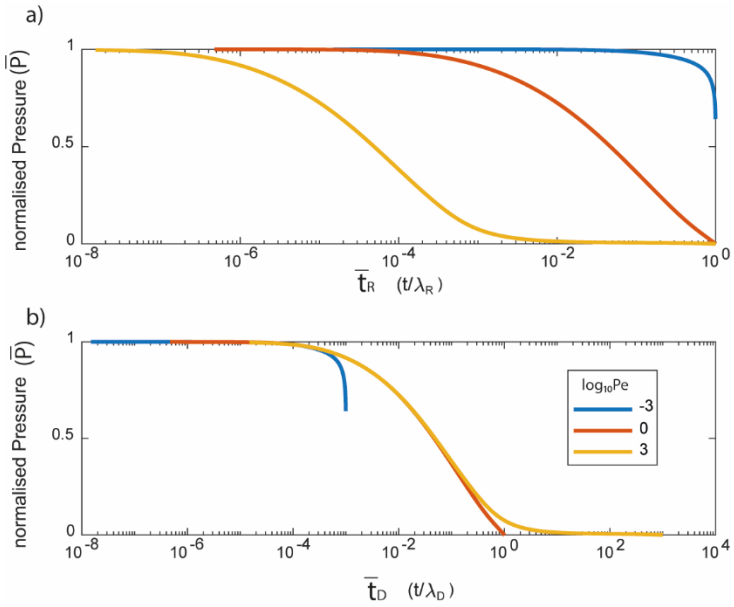

Figure 2.5 evolution of normalised pressure ($\bar{P}$) over a) normalised compression time ($\bar{t_r}$) and b) normalised diffusive time ($\bar{t_D}$). Colours correspond to different Pe simulations specified in table 2.1.

2.5 Parameter testing

I test whether a Pe number under any combination of variables can reproduce the same plots and regimes shown in figure 2.5. I test whether geometric factors such as surface area and total volume, or physical conditions such as H_2O diffusivity, or compression rate summing up to the same Pe values, can reproduce the same behaviour and regimes. Extreme and unrealistic values are considered to test the model's integrity. Compression rates and diffusivities are systematically tested under Pe values at each order of magnitude between 10^{-3}-10^{3}.

Table 2.2 – standard parameters used across the Pe parameter sweeping simulations. Any combination of D and $\dot{R}$ can be taken to produce a single Pe. Each Pe number produces the same normalised results on figure 2.6 for any combination of D and $\dot{R}$to produce the same Pe.

Property	Value [units]
P_{g0}	50 Mpa
T	1173.15 K
A	10^{-5} μm^2
R_0	10 μm
L	90 μm
P_m	2500 Kg/m^3
Pe	10^{-3} - 10^3
C_0	2.53 wt% (Eq. 2.2)
D	1E-11 m^2/s |(Eq. 2.5, rounded)
$\dot{R}$ (dR/dt)	(Eq. 2.11, Pe dependent)

2.5.1 Varying Diffusivity and compression rate

Firstly, figure 2.6 demonstrates that a Pe number can describe the pressure evolution of the system, regardless of what combination of variables are used to calculate Pe. A range of different diffusivity D and compression rate $\dot{R}$ combinations are tested under the same initial geometry and consolidated into a Pe number simulation. These are compared to standard variables (table 2.2) where the Pe variability is only dependent on $\dot{R}$. The solid curves represent benchmark variables where $D = 1 \times 10^{-6}$ and $\dot{R}$ is varied to produce Pe values between 10^{-3}-10^3, in increments one order of magnitude apart. Dashed curves represent any random combination in values of D and $\dot{R}$ to produce the same range of Pe values. The results show that changing D and $\frac{dR}{dt}$ produce no variability between the solid and dashed curves for the same Pe, therefore any quantitative rates of magma compression and diffusion can reproduce predictable results if Pe is known. The highest Pe curves of $\log_{10} Pe = 3$ produce the same high Pe curve shown in figure 2.5 and acts as a 'master curve'. High Pe simulations where $Pe > 1$ stay close to the 'master curve'. In contrast, $Pe \leq 1$ simulations produce curves which fall off the 'master curve' as also shown in figure 2.5. The lower the Pe, the earlier the curves deviate from the 'master curve'.

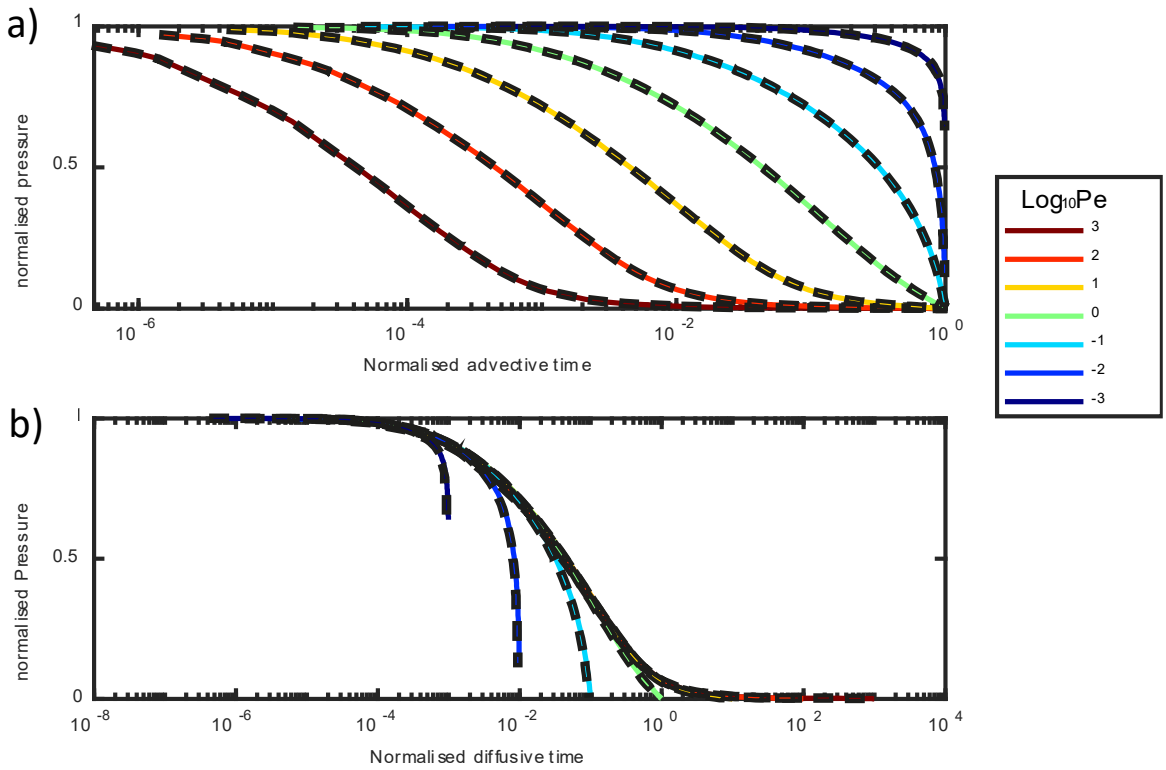

Figure 2.6. Normalised pressure (eq. 2.10) over a) normalised time (eq. 2.11) and b) diffusive time (eq. 2.12), colour coordinated to Pe. Solid lines represent the standard values specified in table 2.2. Dashed outlined curves show results over several combinations of D & dR/dt consolidated to a Pe number for each simulation.

Varying melt and gas volumes

The standard curves (table 2.2, figure 2.7 solid lines) are compared to Pe values calculated at different values for R_0 and L. Different combinations of R_0 and L can lead to different values of initial gas volume fraction ϕ, whilst maintaining a constant Pe. Varying ϕ would change the total number of H_2O molecules in the gas phase which would therefore mean the total number of H_2O molecules in the system (dissolved + exsolved) also varies. It is found that when varying ϕ, the normalised plots shift systematically with ϕ, with lower ϕ producing faster resorption rates compared to compression rates on the advective timescale; the opposite is observed at higher ϕ values (Figure 2.7a). Varying ϕ also produces different curve clusters on the diffusive timescale which shift left or right dependent at lower and higher ϕ respectively (Figure 2.7b). Beginning with the highest Pe The same rules as figure 2.6b apply where when $Pe \gg 1$ produce the full sigmoidal 'master curve' and lower $Pe \ll 1$ fall off the master curve of each ϕ . The curves are not affected when varying D and $\frac{dR}{dt}$ at each ϕ simulation at constant ϕ. Therefore, porosity and

maximum number of moles in the system act as natural scalers to the diffusive system which can affect the overall pressure regime of the system. This is interpreted as gas-liquid systems with a low initial ϕ have more volume of melt for H_2O to be resorbed and stored in, H_2O resorption and diffusion is therefore more efficient and occurs quicker, so equilibrium is reached sooner. On the other hand, when the initial ϕ is higher, more H_2O molecules need to be resorbed in a smaller solvent melt volume, therefore equilibrium is reached slower and at higher P_g due to the higher solubility required to dissolve more H_2O molecules. I also find that varying A whilst maintaining a constant ϕ produces no difference on the normalised plots as the ratio between the gas and melt volumes remain unaffected.

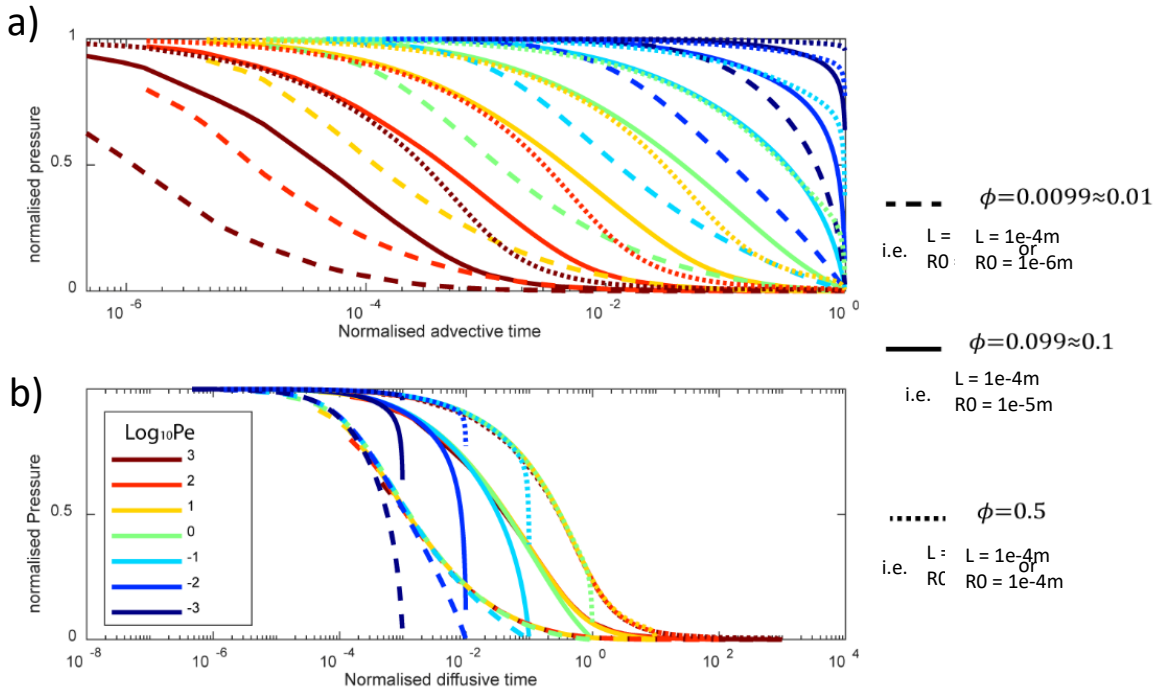

Figure 2.7. over a) normalised time (eq.2.11) and b) diffusive time (eq.2.12), colour coordinated to Pe. Solid lines represent the standard values and initial gas fraction specified in table 2.1. Dotted lines show the results for a smaller initial gas volume fraction. Dashed line shows the results for higher initial gas volume fractions.

2.6 Discussion

The model introduced in this chapter limitations and oversimplifications that seemingly makes it incomparable to natural magma. Notably the cylindrical geometry of the experiment does not represent a bubble suspended in a magma. However, this simplified system provides important insight to volatile dynamics in a closed gas-solvent liquid system by simplifying a difficult problem. The cylindrical geometry, along with the assumption that D is set as constant, also made it possible for Pe to stay constant throughout the

experiment as opposed to a time-varying Pe that a spherical bubble with a H_2O concentration dependent D would bring (see chapter 3).

The main purpose of this model is to gain insight on the evolution of gas-liquid systems under compression. Calculation of a Pe number creates a conceptual framework for the physics that underpin the system, in which we find that the balance between advection and diffusion rates are important. Looking at the normalised pressure curves (Figures 2.3, 2.4, 2.5), we can clearly identify $Pe >> 1$ simulations reach the equilibrium solutions quickly, this is graphically represented by a strong sigmoidal shaped curve that plateaus at $\bar{P}$*=0* before $\bar{t}_R$*=1* (Figure 2.6a & 2.7a) and on the diffusive timescales where the curves follow the shape of the 'master curve' without falling off (Figures 2.6 b & 2.7b).

Increasing the initial porosity of the system whilst maintaining a constant Pe increases the time for the pressure to reach equilibrium regime, which is shown on the master curve where $\bar{P}$ is at higher values when $\bar{t}_D$ exceeds 1 despite having high Pe values (Figure 2.5b). A physical interpretation of this is that at high initial porosities the amount of melt available to resorb the H_2O is proportionally less thus increasing the solubility pressure required to resorb higher concentrations of H_2O. The opposite is true when initial porosity is low where resorption is more efficient due to a lower concentration requiring lower solubility pressures in the melt.

On the other extreme, where $Pe << 1$, the normalised pressure to normalised time plots produce a 'bullnose' curve rather than a sigmoidal curve. On the advective timescales, normalised pressure is non-zero *at* $\bar{t}_R$*=1* and the curves fall off the master curve on the diffusive timescales (Figures 2.5, 2.6 & 2.7), which can be interpreted as incomplete diffusion at the end of the experiments where there are significant number of moles of gas left in the melt undissolved so the pressure in the gas tends to infinity. A transitional regime can be observed when $10^{-1} \leq Pe \leq 10$ where the curves reach or are close to $\bar{P}$*=0* but do not make a strong sigmoidal curve on the advective timescale and falls off the master curve.

The most important insight gained from varying the components of Pe is that the D and $\frac{dR}{dt}$ are the main parameters that decide which Pe regime the system will be in. But using any variation of D and $\frac{dR}{dt}$ will not affect the normalised pressure results so the pressure evolution is predictable. A high initial gas fraction has less solvent space compared to the total number of volatile molecules so diffusion is less effective, and supersaturation may be reached, regardless of the Pe number. Low initial porosities have more solvent space compared to the total number of volatile molecules, so diffusion is more effective.

2.7 Conclusions and next steps

In natural magma chambers, if we assume a constant diffusivity within the melt, the main driver for deciding the Pe regimes will be the initial porosities and the compression rates. The advantages of using the equilibrium solutions are that calculations are less computationally costly and can be calculated quickly. However, we have established the theoretical possibility that when the magma compression rates are fast enough, the dissolution of volatiles may not be able to keep up with the volumetric compression rate which could cause the pressure to get significantly higher than the equilibrium solution. A hypothesis also arises where greater magma porosities may more easily reach this pressure disequilibrium when being compressed because there is proportionately less space for volatiles to be dissolved in. Following on from this investigation, the model will be adapted and improved to resemble a bubbly magma more accurately, considering the spherical dimensions of bubbles. The current model only measures the gas pressure but does not quantify the force required to push the liquid piston arm to produce the given compression rates. This would require more variables to be considered, most importantly: the viscous resistance of the melt and the pressure due to surface tension arising from the spherical shape of the bubble. Understanding and quantifying the importance of viscosity and surface tension pressure will be important in unravelling the pressure evolution on a compressing magma when a volume change is known.

3 – Compression of a spherical bubble surrounded by an incompressible fluid and the effects of surface tension and viscous resistance

The previous chapter has highlighted the importance of volatile diffusion in controlling the pressure of a compressing gas. The 'piston' model previously used, whilst providing a simplified view of the problem, is crucial for understanding the fundamental processes that control the gas pressure in a closed gas-liquid system undergoing compression and diffusion-mediated resorption. A central focus of the previous chapter was describing the pressure evolution regime of a compressing gas-liquid system with a non-dimensional Pe number (Eq. 2.12), which is the ratio between an advective timescale (λ_R) and a diffusive timescale (λ_D):

$$Pe = \frac{\lambda_R}{\lambda_D}$$

Three pressure evolution regimes were identified in the previous chapter: The high Pe $(Pe \gg 1)$ 'equilibrium' regime where the timescale of gas compression is longer than the timescale of volatile diffusion through the melt $(\lambda_R > \lambda_D)$, resulting in efficient resorption and gas pressure evolving at equilibrium with volatile solubility. The low Pe regime $(Pe \ll 1)$ 'Limited resorption' where the timescale of gas compression is shorter than the timescale of volatile diffusion through the melt $(\lambda_R < \lambda_D)$, resulting in limited resorption, and higher pressure due to more molecules remaining in the gas phase. Finally, a transitional regime where the timescale of gas compression and volatile diffusion are similar $(\lambda_R \approx \lambda_D)$, where volatile resorption cannot fully keep up with solubility resulting in the pressure evolution beginning to deviate from the equilibrium regime towards the no diffusive flux regime.

While the cylindrical model was useful for understanding the fundamental processes of a compressing gas-liquid system in a simplified setting, its usefulness for describing natural processes is limited by simplifying factors, most notably:

1. The geometry does not well represent bubbles in magma which would have spherical bubbles suspended in melt. A new approach to solve the system of equations for a spherical geometry is required.
2. The micro-scale spherical geometry of real bubbles in a magma chamber is ignored, hence, surface tension acting on the bubble was omitted.
3. Viscous resistance from the melt surrounding the bubbles have not been accounted for.
4. The melt shell thickness would change due to changing bubble volume in order to conserve incompressible melt volume.
5. H_2O concentration dependent physical properties such as viscosity and diffusivity have been omitted.

This chapter addresses these above limitations posed by the previous model to resemble natural processes more closely.

We begin from fundamental processes of gas-liquid systems. The Rayleigh-Plesset equation describes the fluid dynamics of a spherical bubble suspended in an incompressible fluid, equation 3.1 shows a modified version of the Rayleigh-Plesset equation that describes the pressure of the system, i.e. the total pressure acting at the outer boundary of the shell (P_∞), is equal to the sum of the gas pressure$\left(P_g\right)$, the surface tension acting on the bubble (P_σ) and the viscous resistance from the melt $\left(P_\eta\right)$:

$$P_\infty = P_g - P_\sigma + P_\eta. \qquad \text{(Eq. 3.1)}$$

One can quantify the evolution of P_g by the same method as the previous chapter using the ideal gas law in a spherical bubble. The latter two quantities (the Laplace pressure and the viscous pressure) have been omitted in the previous model for simplicity, however they may be important quantities in calculating the pressure evolution of the system. The surface tension acting on the bubble (P_σ) be considered a negligible component in determining the pressure evolution of a gas-liquid system, especially for larger bubble volumes, some studies have omitted the effects of P_σ entirely for this reason (Blower et al., 2001). However, the effects of surface tension cannot be entirely neglected for shrinking as the surface tension increases towards infinity as a bubble shrinks towards zero radius. Viscous resistance from the liquid $\left(P_\eta\right)$ may also play a significant role in the calculation of the pressure of a bubbly

magmatic system, particularly shallow, silica-rich magmas where their viscosities are strongly sensitive to H_2O concentrations. The sign preceding P_η is dependent on whether we are expanding or compressing the bubble, but in this model stays positive as we only consider compression of bubbles. A rhyolite can vary viscosity between 10^4-10^{11} Pas due to dissolved H_2O concentration between 0-12wt% at a constant temperature of 1200°K (Hess and Dingwell, 1996; Giordano et al., 2008). As H_2O is resorbed into the melt due to compression, we can expect the viscosity of the melt to also decrease.

3.1 Model setup and methods

In this model, the 'bubble cell' model approach by Prousevitch et al (1993) is adopted. A bubbly magma is approximated into a lattice of 'bubble cells', where all of the bubble cells in the lattice are identical and deform homogenously throughout all cells in the lattice. Each bubble cell is composed of a spherical bubble surrounded by a finite volume of incompressible melt. Individual cells do not interact with others (Figure 3.1). The key advantage of this approach is that modelling the behaviour of a single bubble can reflect the average processes across an entire magma body. Furthermore, assuming radially symmetric processes across a bubble cell, 1-D modelling of the radius of a single bubble cell is possible to describe the processes of a magma body.

In this chapter we will focus on the deformation of a single bubble under the constraints of a constant compression rate producing a linear compressive timescale (λ_R), an isothermal temperature and a perfectly closed system. In this chapter, we will define a "system" referring to a single bubble-melt cell within the lattice, which approximates the processes of all bubbles across the bubble cell lattice.

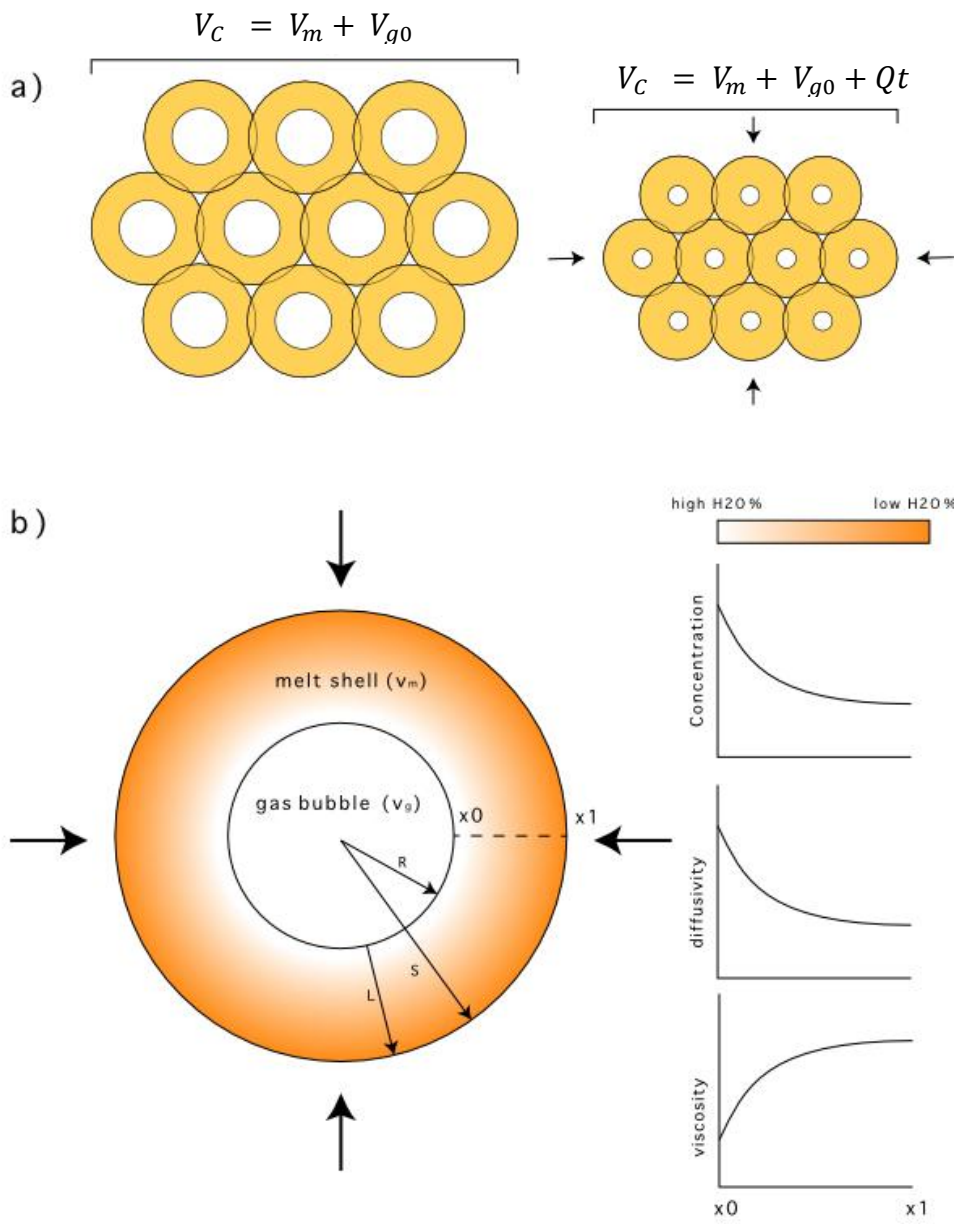

Figure 3.1 Schematic illustrations of the bubble cell lattice model (Prousevitch et al., 1993b). *(a) illustrates the distribution of the bubble cells on the lattice. The system-scale volume balances when applying a volumetric compression Qt of total (melt + gas), melt and initial gas volumes are notated as V_C, V_m & V_{g0} respectively are shown. (b) shows the geometry and lengths of an individual bubble cell, graphs show the expected trends shown through the melt shell during the compression of a bubble cell. Individual bubble-scale volumes are notated by lowercase values v_c, v_m & v_{g0} for the total, melt and initial gas volumes respectively. Characteristic lengths on the bubble scale include bubble radius R, melt shell thickness L and total cell thickness $S = R + L$.*

3.1.1 Geometric relationships

The first key difference between this model and the piston model presented in chapter 2 is the difference in geometric relationships for spherical bubbles. When a bubble is compressed, the volume and radius of the gas bubble decreases so the melt shell thickens to conserve the volume of the incompressible melt. Applying a constant volumetric compression rate Q towards a total compression timescale λ_R (when the initial gas volume v_{g0} is completely compressed ($v_{g0} = Q\lambda_R$)), the volumetric relationships of the bubble cells are described below:

$$v_c = v_{g0} + v_m - Qt, \quad \text{(Eq. 3.2)}$$

where v is volume, and subscripts c, g & m represent the cell, gas bubble and melt shell respectively. Subscript zero notates initial values. As the gas is the only compressible phase, the bubble volume at any time can be calculated as:

$$v_g = v_{g0} - Qt. \quad \text{(Eq. 3.3a)}$$

Note that $v_{g0} = v_c\phi_0$ and $v_m = v_c(1 - \phi_0)$, hence the above equation can be rewritten in terms of initial gas fraction ϕ_0:

$$v_g = v_c\phi_0 - Qt. \quad \text{(Eq. 3.3b)}$$

Thus, the bubble radius R can be expressed as:

$$R = \left(\frac{3(v_c\phi_0 - Qt)}{4\pi}\right)^{\frac{1}{3}}, \quad \text{(Eq. 3.4)}$$

assuming the bubble is a perfect sphere throughout. Thus, the radial compression rate $\dot{R}$ (dR/dt) can be solved analytically when differentiating R with respect to time:

$$\frac{dR}{dt} = \dot{R} = -Q\left(\frac{1}{36\pi(v_c\phi_0 - Qt)^2}\right)^{\frac{1}{3}}. \quad \text{(Eq. 3.5)}$$

Note that the above equations are only valid for a constant Q. The compression of the bubble volume Q causes a reduction in the gas volume Δv_g which is driven by an increasing ambient pressure P_∞ which is one of the main outputs of the model.

The change in length scales relevant to the system with respect to the volumetric relationships in equations 3.1-3.4 are given as:

$$v_g + v_m = \frac{4}{3}\pi S^3 = \frac{4}{3}\frac{\pi R^3}{\phi},\ S = R\phi^{-\frac{1}{3}} = L + R\ , \quad \text{(Eq. 3.6)}$$

where L is the thickness of the melt shell surrounding the bubble, distinct from S which is the total radius of the bubble cell (melt+bubble); see figure 3.1b.

3.1.2 Numerical setup

This study modifies the numerical model by Coumans *et al.* (2020). The model is the latest iteration in a series of numerical models that solve the hydrodynamics of the bubble cell model (Prousevitch et al., 1993b; Lyakhovsky et al., 1996; Proussevitch and Sahagian, 1998; Blower et al., 2001), and provides a user friendly, open source code. The hydrodynamic equation from Coumans *et al.* (2020) is rearranged to the format of (Eq. 3.1) to output P_∞ under a forced change in volume described in equations 3.2 – 3.5. The full form of equation 3.1 can be written with the assumption that viscosity is spatially constant throughout the melt shell (Prousevitch et al., 1993b):

$$P_\infty = P_g - \frac{2\sigma}{R} - 4\eta\frac{dR}{dt}\left(\frac{1}{R} - \frac{R^2}{S^3}\right), \quad \text{(Eq. 3.7a)}$$

where the rightmost term represents viscous resistance and surface tension acting on the bubble:

$$P_\eta = 4\eta\frac{dR}{dt}\left(\frac{1}{R} - \frac{R^2}{S^3}\right), \quad \text{(Eq. 3.7b)}$$

$$P_\sigma = \frac{2\sigma}{R}, \quad \text{(Eq. 3.7c)}$$

where η is the melt viscosity [Pas] and σ is the surface tension [N/m]. Each pressure constituent has been carefully experimentally validated by Coumans *et al.* (2020). Alternatively, equation 3.1 can be written in terms of a spatially varying viscosity throughout the melt shell (Blower et al., 2001; Coumans *et al.*, 2020):

$$P_\infty = P_g - \frac{2\sigma}{R} - 12R^2\frac{dR}{dt}\int_{R_0}^{S_0}\frac{\eta(x)x^2}{\left(R^3 - R_0^3 + x^3\right)^2}dx, \quad \text{(Eq. 3.8a)}$$

where:

$$P_\eta = 12R^2\frac{dR}{dt}\int_{R_0}^{S_0}\frac{\eta(x)x^2}{\left(R^3 - R_0^3 + x^3\right)^2}dx. \quad \text{(Eq. 3.8b)}$$

The melt shell coordinates are constrained between the initial bubble radius R_0 and initial total cell radius S_0. Similarly to the previous chapter, three solutions are calculated simultaneously to compare with one another. The two analytical end-member solutions

from the previous chapter are reintroduced and modified in this chapter to conform with a spherical geometry; the equilibrium and no-diffusive flux end members represent the minimum and maximum pressure evolutions of the gas bubbles respectively. The end members will use the form of equation 3.7a to solve the hydrodynamics of the bubble cell as the melt shell H_2O concentration profile is expected to be spatially constant at any time, neglecting the need to consider spatially dependent viscosity.

A third, full numerical solution will also be calculated which will be compared with the output pressures of the two analytical end-member solutions. The full numerical solution will calculate the spatial and temporal evolution of H_2O across the melt shell L resulting from diffusive processes. This will use equation 3.8a to solve the hydrodynamics of the bubble as spatially variable H_2O concentration across the melt shell will cause the viscosity to vary spatially across the melt shell.

Below I list the following equations that are consistent throughout the three solutions. For all solutions, P_g is simply calculated by the ideal gas law as a function of the number of exsolved H_2O molecules and the volume of the gas bubble:

$$P_g = \frac{8.314 n_g(P_g) T}{v_g}. \quad \text{(Eq. 3.9)}$$

The bubble volume $v_g(t)$ is calculated at each time by equations 3.3a & b and is consistent throughout the three solutions. The initial exsolved H_2O concentration in the bubble is calculated at equilibrium with the initial ambient pressure $P_{\infty 0}$ and pressure due to surface tension $P_{\sigma 0}$ at t=0 ($P_g = P_\infty + P_\sigma$, rearranged from equation 3.1 when $P_\eta = 0$):

$$n_{g0} = \frac{(P_{\infty 0} + P_{\sigma 0}) \cdot v_{g0}}{8.314 T}. \quad \text{(Eq. 3.10)}$$

Solubility is calculated at the bubble-melt interface as a function of the bubble pressure and is consistent throughout the three solutions. The solubility equation is carried over from the previous chapter and is repeated here for clarity (Eq. 2.3, Liu et al., (2005)):

$$C_s = \frac{\left(354.94 {P_g}^{0.5} + 9.623 P_g - 1.5223 {P_g}^{1.5}\right)}{T} + 0.0012439 {P_g}^{1.5}. \quad \text{(Eq. 3.11)}$$

The dissolved H_2O concentration in the melt becomes more significant in this model as we include the dependence of diffusivity and viscosity on dissolved H_2O wt% in the melt.

Diffusivity is a function of ambient pressure P_∞, temperature T and dissolved H_2O concentration C for metaluminous rhyolite melts (Zhang & Ni, 2010):

$$D = C\,exp\left(-18.1 + 1.888P_\infty - 1000\frac{9699+3626P_\infty}{T}\right). \quad \text{(Eq. 3.12)}$$

Viscosity is also strongly dependent on the dissolved H_2O concentration in the melt. We use an empirical parameterisation calibrated for specified melt compositions and dissolved H_2O concentrations (Giordano et al., 2008):

$$log_{10}\,\eta = J_1 + \frac{J_2}{T - J_3}, \quad \text{(Eq. 3.13)}$$

where J_1, J_2 & J_3 are parameters dependent on melt composition (which must be specified) and C.

3.1.3 End member solution 1 – No diffusive flux

The calculation of the first end-member solution is approached similarly to the previous chapter. Here the initial moles of H_2O in the gas phase remains the same throughout compression $\left(n_g \equiv n_{g0}\right)$. Therefore gas pressure evolution is only calculated due to changing gas volume. Also, we consider the melt shell to retain its initial uniform concentration profile as no diffusion occurs in the melt, therefore, we can set a constant melt viscosity throughout time based on the initial melt concentration (Eq. 3.13).

As the H_2O molecules in the melt and gas remain constant spatially and temporally, the no diffusion end-member solution uses the hydrodynamic equation form of equation 3.7. We expect this solution to reflect the maximum possible pressure evolution of the system as P_g trends to infinity as the bubble shrinks and no gas molecules are removed from the bubble. The pressure components for this end-member solution is represented with the brackets $'(1)'$ for analysis (i.e. $P_\infty(1)$).

3.1.4 End-member solution 2 – equilibrium solubility

This method assumes resorption of H_2O instantaneously in equilibrium with compression; this is equivalent to setting $D = \infty$ on the full numerical solution. Gas pressure can be calculated as an implicit product of the ideal gas law (Eq. 3.9) where n_g is calculated at equilibrium to P_g:

$$n_g = n_{g0} + \Delta n_g = n_{g0} - \frac{[C(P_g) - C_0]}{100}\frac{1000\rho_m v_m}{18.015}, \quad \text{(Eq. 3.14)}$$

where C is calculated at each timestep by equation 3.10. P_g is calculated implicitly by finding the roots of equation 3.8. In MATLAB this is done using the 'fzero' function and setting the output to P_g. In the equilibrium solution, C does not vary spatially across the melt shell so the $C(P_g)$ at each timestep from equation 3.13 is carried forwards to calculate η (Eq. 3.13), P_η and P_∞ (Eq. 3.7). The brackets '(2)' are used to label the outputs of this solution for analysis (i.e. $P_\infty(2)$).

3.1.5 Solution 3 – full diffusion coupled numerical solution

The third solution considers the diffusion of H_2O across the melt and most closely resembles natural processes. Here we consider a spatially varying H_2O across the melt shell over time as H_2O is diffused from the bubble to the far edge of the melt shell. Solving diffusion in a bubble cell is approached slightly differently than the previous chapter which maintained a constant volume and thickness of the liquid; assuming incompressible melt, the bubble cell model maintains a constant melt volume, but the thickness of the melt shell increases as the bubble volume shrinks to preserve the melt volume. Therefore, a Lagrangian coordinate system is used to maintain a constant coordinate system (x) for a changing Eulerian lengthscale (A) to calculate the H_2O diffusion. The volume conservation for a Lagrangian coordinate system relative to an eulerian corrdinate system is described by:

$$A^3 - R^3 = x^3 - R_0^3, \qquad \text{(Eq. 3.15)}$$

where R is calculated from equation 3.4 and R_0 is calculated at the initial conditions. The Langrangian system also accounts for the change in dissolved H_2O in the melt with respect to changing coordinates x as part of the volume conservation. One-dimensional H_2O diffusion through the melt shell with spatially varying diffusivity is solved using Fick's second law of diffusion in spherical geometry using the Lagrangian coordinate system:

$$\frac{\partial C}{\partial t} = \frac{1}{x^2}\frac{\partial}{\partial x}\left(D\frac{A^4}{x^2}\frac{\partial C}{\partial x}\right), \qquad \text{(Eq. 3.16)}$$

where D is a vector calculated in (Eq. 3.12) using the vector for C in Lagrangian form from the previous time-step. The boundary condition for (Eq. 3.16) is set as the solubility due to

the current gas pressure at the bubble wall (Eq. 3.11) and a zero gradient outer boundary condition reflective of an adjacent bubble in the lattice:

$$C = C_s(P_g)\,|_{x=0},$$
$$\frac{\partial C}{\partial x} = 0\,|_{x=1}.$$

This results in H_2O diffusing from the bubble to the far edge of the melt shell. The gas pressure is calculated by the number of moles remaining in the gas at time, this is done by trapezoidal integration of the current H_2O concentration profile and calculating its difference to the initial concentration profile:

$$n_g(t) = n_{g0} + \Delta n_g = n_{g0} + \frac{4\pi\rho_m}{18.015\times100}\left(\int_{R_0}^{S_0} C(x,0)x^2\,dx - \int_R^S C(x,t)x^2\,dx\right), \quad \text{(Eq.3.17)}$$

where ρ_m is the melt density in kg/m^3 and Δn_g is negative. Finally, the melt viscosity η is a spatially varying vector calculated from the vector C (Eq. 3.13), the viscosity can then be inputted into equation 3.8 to calculate P_η due to a spatially varying melt viscosity.

This numerical framework is setup in MATLAB where the spatial derivatives and finite differences, (specifically Eq. 3.16) are approximated by MATLAB's built in ODE15s solver (Shampine & Reichelt, 1997) which also resolved non-linear iterations to appropriate tolerances (Absolute = 10^{-6}, Relative = 10^{-4}). The pseudo-code for the numerical solution is available in the appendix.

3.2 Analysis methods

We use a similar method to compare the numerical results to the analytical end-member solutions as the previous chapter, where a Peclet number (Pe) can describe the pressure evolution regime of the system. The equation calculating Pe at any time is a ratio of the diffusive viscous timescales:

$$Pe = \frac{\lambda_r}{\lambda_D}, \quad \text{(Eq. 3.18)}$$

where λ are the quantitative timescales of advection (subscript r) and diffusion (subscript D) in seconds.

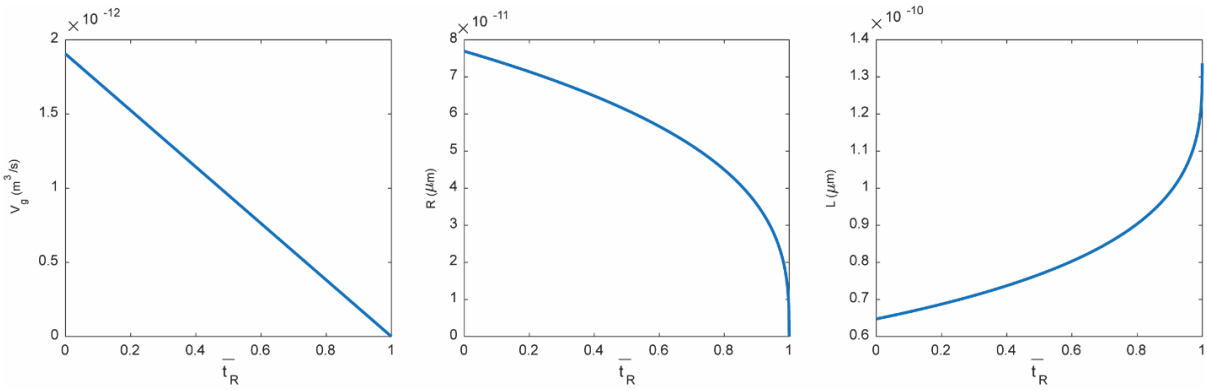

Figure 3.2. The evolution of gas volume v_g, bubble radius R and melt shell thickness L over normalised time $\bar{t_r}$ (equation 3.19). Results are specific table 3.1 which would all show the same profiles over normalised time.

Due to the spherical geometry of the bubbles, when a bubble is being compressed at a constant volumetric compression rate of Q, the radial compression rate $\dot{R}$ is not constant but increases in magnitude as the bubble gets smaller, an example of this effect is shown in figure 3.2. This gives a non-constant radial compression timescale:

$$\lambda_r = \frac{R}{\dot{R}}, \qquad \text{(Eq. 3.19)}$$

where $\dot{R}$ is $\frac{dR}{dt}$. For simpler quantification of advective timescales, we use a constant characteristic advection timescale $\overline{\lambda_r}$ based on the initial relevant geometric parameters of the bubble (Q_C, v_c, ϕ_0). A linearised normalised advective time between 0 and 1, can be obtained by dividing dimensional time with the characteristic advective timescale:

$$\bar{t_r} = \frac{t}{\overline{\lambda_r}} = \frac{tQ_C}{v_c\phi_0}, \qquad \text{(Eq. 3.20)}$$

where:

$$\overline{\lambda_r} = \frac{v_c\phi_0}{Q_C}.$$

In terms of the diffusive timescale, since $D(t)$ is a vector of concentration dependent diffusivity across the melt shell at any given time, the diffusivity must be averaged across the melt shell to obtain an average or effective diffusivity $\overline{D}$. The use of the lagrangian coordinate system from equation 3.15 for the melt shell means an extra step of dimensionalising the melt spatial vector is required:

$$\overline{D} = \frac{1}{\frac{4\pi A_f^3}{3} - \frac{4\pi A_0^3}{3}} \int_{A_0}^{A_f} 4\pi A^2\, D(A) dA = \frac{3}{\left(A_f^3 - A_0^3\right)} \int_{A_0}^{A_f} A^2\, D(A) dA, \qquad \text{(Eq. 3.21)}$$

where A is obtained by rearranging equation 3.15

$$A = \sqrt[3]{x^3 - R_0^3 + R^3},$$

And initial D at $t = 0$ is a constant value dependent on the assuming a uniform C throughout the melt shell (Eq. 3.12). Effective diffusivity $\overline{D}$ along with the temporally thinning melt shell thickness L can be used to calculate a diffusive time normalisation:

$$\bar{t}_D = \frac{t}{\lambda_D} = \frac{t\overline{D}}{L^2}. \quad \text{(Eq. 3.22)}$$

For spherical dimensions, the melt shell thickness L increases over time as the bubble shrinks (Eq. 3.6) and the effective diffusivity $\overline{D}$ also changes over time; therefore, the diffusive timescale $\lambda_D$is time dependent and is calculated at each timestep. Like the previous chapter, if a plot exceeds $\bar{t}_D \geq 1$, H_2O diffusion and resorption can be considered to occur fast enough for solution 3 to reach the equilibrium pressure during compression. If $\bar{t}_D < 1$, H_2O diffusion cannot keep up with pressurisation due to bubble shrinkage, thus increasing the overall pressure towards the no diffusion regime. I compare the results from the full numerical solution with the equilibrium and no diffusive flux solutions to see the evolution of the pressure regimes during compression:

$$\overline{P_g} = \frac{P_g - P_g(2)}{P_g(1) - P_g(2)} \quad \text{(Eq. 3.23)}$$

Looking back at the hydrodynamic equation (equations 3.1, 3.6 & 3.7) we expect that for any combination of variables, P_g will increase but also P_σ will increase as R gets smaller. When gaseous H_2O in the bubble resorbs, we expect P_η to vary in every simulation as the dissolved H_2O concentration will increase, decreasing the viscosity (equation 3.13). The effect of decreasing viscosity is opposed by an increase in $\frac{dR}{dt}$ which becomes greater (more negative) over time. Therefore, in the no diffusion case where η doesn't vary due to dissolved H_2O, P_η is expected to be greater (more negative) than the other solutions where H_2O is resorbed. It will also be valuable to assess the relative importance of viscous resistance and surface tension when pressurising a system. P_g, P_σ & P_η can all be considered as individual components that make up the output P_∞. Ultimately, we care about P_∞ the most as it reflects the pressure evolution of the magma to produce the compression Q. We

expect higher P_η to increase P_∞ because $\frac{dR}{dt}$ is negative, whereas we expect higher P_σ to decrease P_∞. The balance of P_η &P_σ will determine whether the output P_∞ will be greater or less than P_g. When $P_\sigma > P_\eta$, this will cause P_g to be undepressured compared to P_∞. The model will however stop when the bubble radius reaches a minimum value of 1µm to ensure model stability by preventing infinitesimally low bubble radii.

3.3 Parametric study

This model has been used to systematically test a wide range of variables to identify diffusive regimes, the effects of viscous resistance and surface tension. The following investigations are laid out to incrementally increase complexity of the model. Each additional complexity added to the model will be assessed for its impact on the overall pressure of the system. The series of investigations are done in the following order:

- Isolating P_g to see whether Pe number analysis can be used to identify the diffusive regimes for the spherical shell model. Results should agree with the simplified cylindrical model from the previous chapter but how does using spherical coordinates differ to the cylindrical model?
- Investigate the effects of the viscous resistance term and the surface tension term (P_η & P_σ) on the overall pressure of the system
- Adding a dissolved H_2O dependent diffusivity and melt viscosity calculations (equation 3.11 & 3.12)

3.4 Identifying diffusive disequilibrium

The first parametric study isolates the gas pressure evolution in order to reproduce the diffusive regimes identified in the previous chapter correlating with a Pe number. As P_g is the only output in this initial investigation, we can omit P_η & P_σ for the time being. Here, the gas pressure evolution is obtained for the 3 solutions under a constant input compression rate Q, which correlates to an advective timescale $\overline{\lambda_r}$. The pressure evolution in terms of Pe are tested by firstly, using constant values for diffusivity across the melt and throughout the simulation times, under a constant Q. Similarly, I vary Q over 6 orders of magnitude under a constant D, where Q is represented by its effective compressive timescale $\overline{\lambda_r}$. From here on, where we define dR/dt is when individual bubble mechanics are described and is directly proportional to Q. The input parameters are listed in the table 3.1:

Table 3.1. Model parameters for the parametric study. Varying diffusivity D uses a constant compression rate Q. Varying compression rate Q, uses a constant diffusivity. Physical parameters used are similar to table 2.1

	Varying D	Varying Q
Initial Total cell volume (v_c)	1×10^{-11} m^3	1×10^{-11} m^3
Diffusivity (D)	10^{-16}-$10^{-8}$$m^2s^{-1}$	1×10^{-12} m^2s^{-1}
Compression timescale ($\overline{\lambda_r}$)	10^8 s	Variable, 1000-10^8 s
Initial Gas volume fraction (ϕ)	0.16	0.16
Initial ambient pressure (P_0)	50MPa	50MPa
Temperature (T)	1000°C	1000°C
Melt density (ρ_m)	2426.5 (Kgm^{-3})	2426.5 (Kgm^{-3})
Surface tension (σ)	0.22 (Nm^{-1})	0.22 (Nm^{-1})

Figure 3.3 plots three simulations from table 3.1 showing the H_2O concentration profiles across L over time, highlighting the 3 gas pressure regimes initially identified in the previous chapter. The figure 3.3 plots are similar to the concentration profiles from the previous chapter and identifies what the gas pressure regimes mean in terms of dissolved H_2O concentrations. Low Pe $(Pe \ll 1)$ produces concentration profiles with steep gradients between the bubble wall ($x = 0$) and the far edge of the melt shell $(x = L)$, diffusivity is much slower than compression, so the H_2O does not diffuse fully through the melt and less H_2O is dissolved (Figure 3.3a). On the other extreme where Pe is high $(Pe \gg 1)$, diffusivity is sufficiently high compared to compression that the concentration profile shifts upwards due to solubility and there is no variation at any time between the concentrations at the bubble wall and edge of the shell (Figure 3.3c). A transitional regime where $Pe \sim 1$ shows that the H_2O dissolves through the melt shell but too slowly to be in equilibrium, so more H_2O molecules accumulate near the bubble wall (Figure 3.3b).

The most notable difference between the figure 3.3 profiles and the concentration profiles from the previous chapter (Figure 2.4), is that the melt shell thickens as the bubble shrinks smaller as represented in figure 2.3. Changes in melt shell thickness is also shown on figure 3.3 where the maximum distance from the bubble increases over time. Another key difference is that as dR/dt increases towards the end of each simulation, the Pe value

subsequently decreases (equation 3.20) which affects the concentration gradients. Figure 3.3b shows the H_2O concentration profile moving further into disequilibrium towards the end of the compression as Pe is decreasing and dR/dt increases.

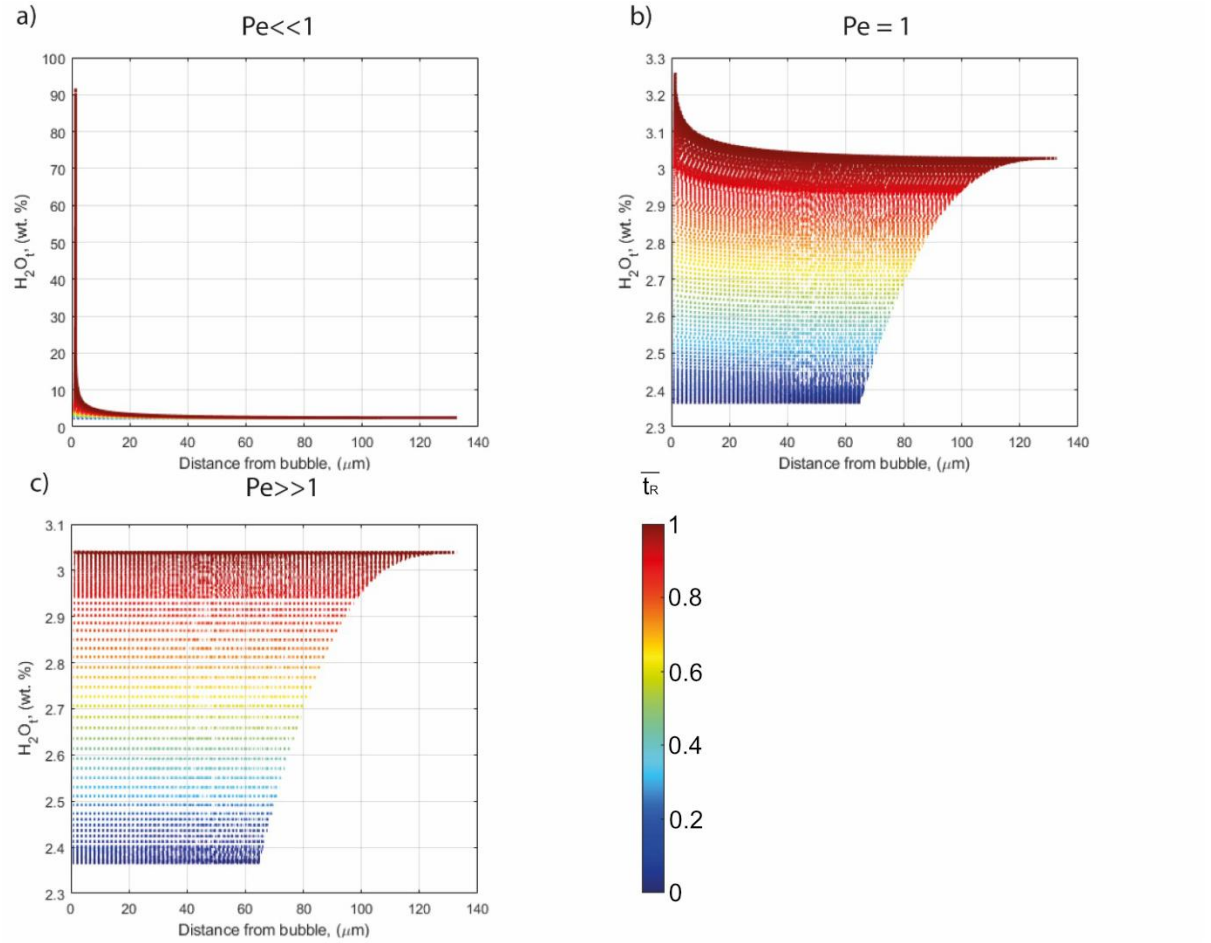

Figure 3.3. The evolution dissolved H_2O concentration profile through the melt shell over normalised time for the 3 Pe regimes, each colour represents a point in time. A) $Pe \ll 1$, diffusion through the melt "throttles" the gas resorption at the bubble wall, pushing the bubble pressure towards the no diffusion end-member solution. B) $Pe \sim 1$, compression and diffusion timescales are similar. The H2O concentration profiles are not in complete equilibrium. C) $Pe \gg 1$, diffusion is sufficiently fast enough to keep at equilibrium with compression, each concentration profile at any time is uniform.

The normalised gas pressure ($\bar{P}_g$) over normalised time plots ($\bar{t}_R$ & $\bar{t}_D$) for the parameters in table 3.1 show sigmoidal plots similar to the normalised plots from the previous chapter. The normalised plots in figure 2.4show that the curves shift systematically with varying diffusivity and compression rate. A sigmoidal curve on the advective timescales (Figure 3.4a & b) is shown when the diffusive timescale is shorter than the compression timescale. The

sigmoidal curves reach a value of $\overline{P_g} = 0$ faster as diffusivity increases showing that gasses

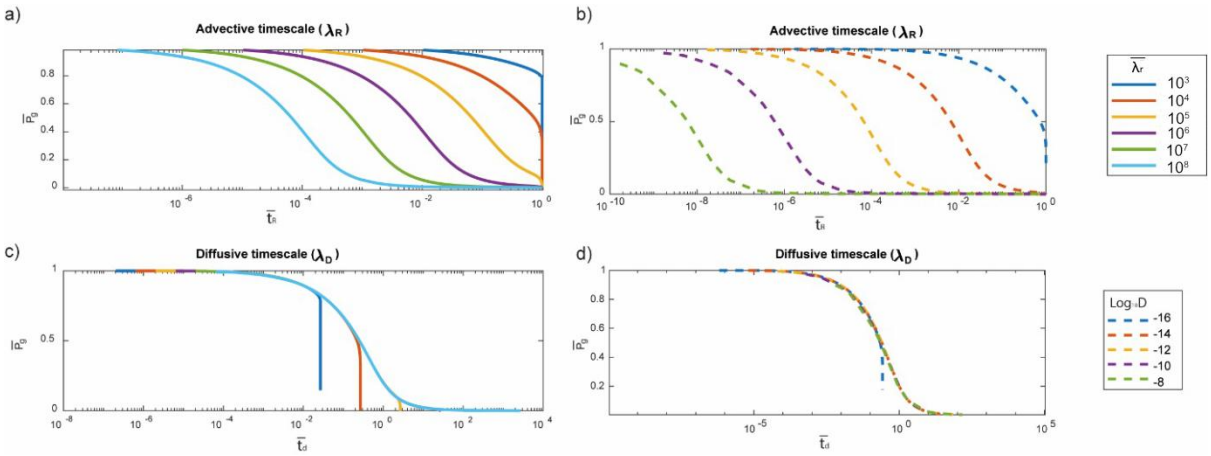

Figure 3.4. Normalised pressure ($\overline{P}$) over normalised time ($\overline{t_R}$ & $\overline{t_D}$) plots for varying diffusivity D (left solid lines; a & c) and varying compression timescales $\overline{\lambda_r}$ due to varying compression rates Q (right, dashed lines; b & d). Results for advective timescales (λ_R, equations 3.1 & 3.2) are shown on the top plots (a & b) and results for the diffusive timescale (λ_D, equation 3.4) are shown on the bottom plots (c & d)

resorb back into the melt quicker as a high diffusivity makes diffusion through the melt more efficient (Figure 3.4a). When diffusion is much slower than compression the normalised curves do not show the sigmoidal shape and $\overline{P_g} > 0$ at the end of the normalised time. The same trends are observed when varying Q at a constant diffusivity, a fast Q equates to a short compression timescale. When the compression timescale is long compared to the diffusive timescale, the compression is slow enough for H_2O to resorb in equilibrium (Figure 3.4b). The diffusive timescales (Figure 3.4c & d) also show similar trends to the previous chapter's cylindrical model where high D compared to Q produce identical curves that fit into a 'master curve' which can be seen on both the varying D and varying Q plots (Figure 3.4c & d). These master curves exceed $\bar{t}_D = 1$ and end at $\overline{P} = 0$ indicating that diffusive resorption occurs quickly enough to keep at equilibrium gas pressure with the compression rate. When diffusion cannot keep up with compression, the curves fall off the 'master curve' and end before $\bar{t}_D = 1$. λ_D dynamically changes over time as L thickens as the gas bubble shrinks, this causes λ_D to increase over the course of each simulation $\left(\lambda_D = \frac{L^2}{D}\right)$.

The dynamic λ_R & λ_D causes the Peclet number (Pe) to evolve over time (equation 3.18) shown in figure 3.5 where for all simulations, Pe decreases rapidly near the end of normalised time indicating that λ_R increases towards infinity. Figure 3.5 also shows that most of the results from table 3.1 start at $Pe \gg 1$ indicating that diffusion occurs at

equilibrium with compression, but all curves end up falling below $Pe = 1$ by the end of the simulations. Therefore, we can conclude that it is a fundamental property for Pe to trend towards zero as a spherical magmatic bubble compresses towards zero radius. This is a fundamental difference between the plots of the previous chapter's cylindrical model and the shell model investigated here. Figure 3.6 also shows that the same Pe curves can be reproduced at different combinations of D & Q at the same initial volumes (e.g. $\log_{10}D$ = -12 & $\log_{10}Q$ = 2) which agrees with the results from the previous chapter. It is expected that the Pe and normalised pressure/time curves will be shifted when using different initial bubble volumes and shell thicknesses.

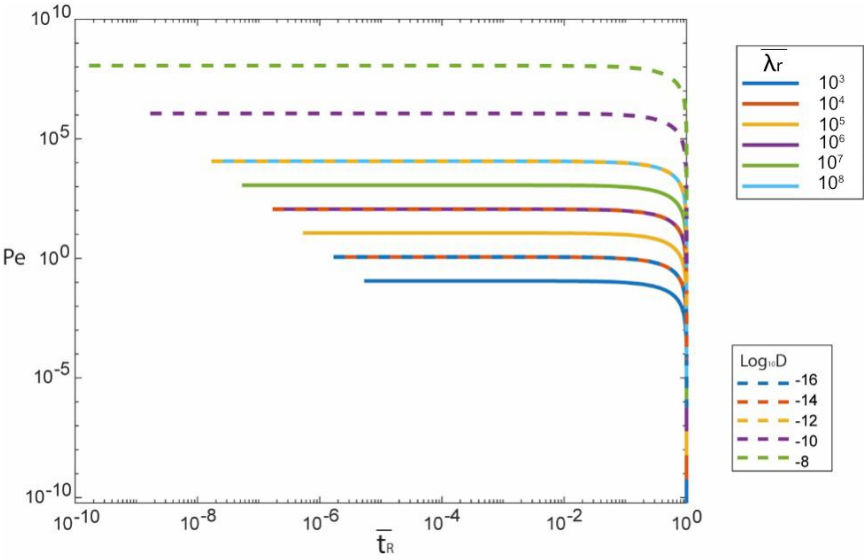

Figure 3.5. Evolution of Pe over normalised time for the results from table 3.1. The normalised time shown is $\bar{t}_R$. Solid lines show results for varying Q, translated into compression timescale $\overline{\lambda_r}$ (equation 3.20). dashed lines show results for varying D.

3.5 Effects of viscous resistance and surface tension

The remaining pressure components of the hydrodynamic equation; P_σ & P_η are the main components that cause the difference in gas pressure and ambient pressure; the hydrodynamic equation is repeated below for clarity:

$$\Delta P = P_g - P_\infty = P_\sigma + P_\eta \, .$$

The bubble overpressure ΔP relates to the difference between the total magma pressure (P_∞) and P_g. Bubble pressure is the sum of the surface tension and viscous resistance pressures acting on the bubble where P_σ acts to favour bubble shrinkage and P_η determines

the direction of radial bubble growth. In the case of bubble compression P_η is always negative due to a negative $\frac{dR}{dt}$. P_σ can be calculated analytically by combining equation 3.3 with the surface tension (Laplace) term (equation 3.7c):

$$P_\sigma = \frac{2\sigma}{R} = 2\sigma\left(\frac{3v_c\phi_0 - Qt}{4\pi}\right)^{-\frac{1}{3}} \quad \text{(Eq. 3.24)}$$

Similarly, P_η can be calculated analytically if viscosity is assumed constant throughout the melt shell and time by combining equations 3.7b & 3.8b with equations 3.3 & 3.4, however the analytical solution derived is too complex to be written out.

Here, I firstly test the effects of viscous resistance when viscosity is spatially and temporally constant. Using the analytical solution for P_η, viscosity is varied over several orders of magnitude and Q is also varied. The output P_η is represented as positive values on figure 3.6 so it can be easily compared with P_σ on the same plot.

Table 3.2. Parameters used to simulate the evolution in viscous P_η and surface tension (Laplace) pressure P_σ. Parameter sweep simulations varying η use a constant Q. Simulations varying Q use a constant η.

	Varying η (Figure 3.6a)	Varying Q (Figure 3.6b)
v_c	1×10^{-11} m^3	1×10^{-11} m^3
ϕ_0	0.16	0.16
$\overline{\lambda_r}$	10^6	10-10^{15} s
Q	$= \frac{v_c\phi_0}{\overline{\lambda_r}} = 1.6e^{-18}$m^{3}s^{-1}	$= \frac{v_c\phi_0}{\overline{\lambda_r}} = 1.6e^{-13}$-$1.6e^{-19}$ m^{3}s^{-1}
σ	0.22	0.22
η	10^2-10^{12} Pas	10^4 Pas

Figure 3.6 plots the results for table 3.2. The Laplace pressure (P_σ) on a normalised timescale produce a single trend across all input parameters. This is because, the bubble radius evolves proportionately on a normalised timescale $\left(\overline{t_r} = \frac{t}{\overline{\lambda_r}}\right)$ when starting from the

same initial bubble radius, and P_σ is inversely proportional to the bubble radius (Eq. 3.7a). If the starting bubble volume is higher or lower, the P_σ profiles would shift downwards and upwards respectively. However, for the given bubble volumes set in table 3.2, the P_σ profiles play a negligible role throughout the simulation time (~0.006MPa) until at low bubble radii where P_σ increases towards infinity following a power law. In nature, this phenomenon drives a bubble to spontaneously contract and disappear due to the high surface tension acting on the tiny bubble. We stop the model at a set minimum bubble radius to prevent the model from producing P_σ values trending to infinity, which would cause the model to be unstable.

The viscous resistance (P_η, note that $-P_\eta$ is plotted in order to be compared with P_σ) profiles also show a power law trend increasing to infinity towards the end of compression. This is due to the radial growth rate $\left(\frac{dR}{dt}\right)$ having a cubic relationship with the constant compression rate Q & v_g (Eq. 3.5), increasing towards infinity at decreasingly low bubble radii. Each P_η profile shown in figure 3.6 shifts upwards and downwards by orders of magnitude proportionally to varying the compression timescales by orders of magnitude (Figure 3.6a) and varying viscosity by orders of magnitude (Figure 3.6b). However, under a wide range of parameters, P_η plays a negligible role in the overall pressure of the system and in many cases is lower than the surface tension pressure. This means that the difference between P_g & P_∞ is dominantly controlled by P_σ. It is only at exceptionally fast compression timescales or exceptionally high viscosities that P_η exceeds P_σ, thus making the difference between P_g & P_∞ viscously controlled. An exception to this would be if the magma bubble number density is much larger (i.e. gasses distributed into more, smaller bubbles), the initial P_σ would start at a much greater value due to the smaller initial bubble radii. Next, we test the full numerical solution (solution 3) with a spatially varying η and using natural parameters to determine whether calculating P_η is worthwhile for calculating P_∞ for natural compressing magmatic systems.

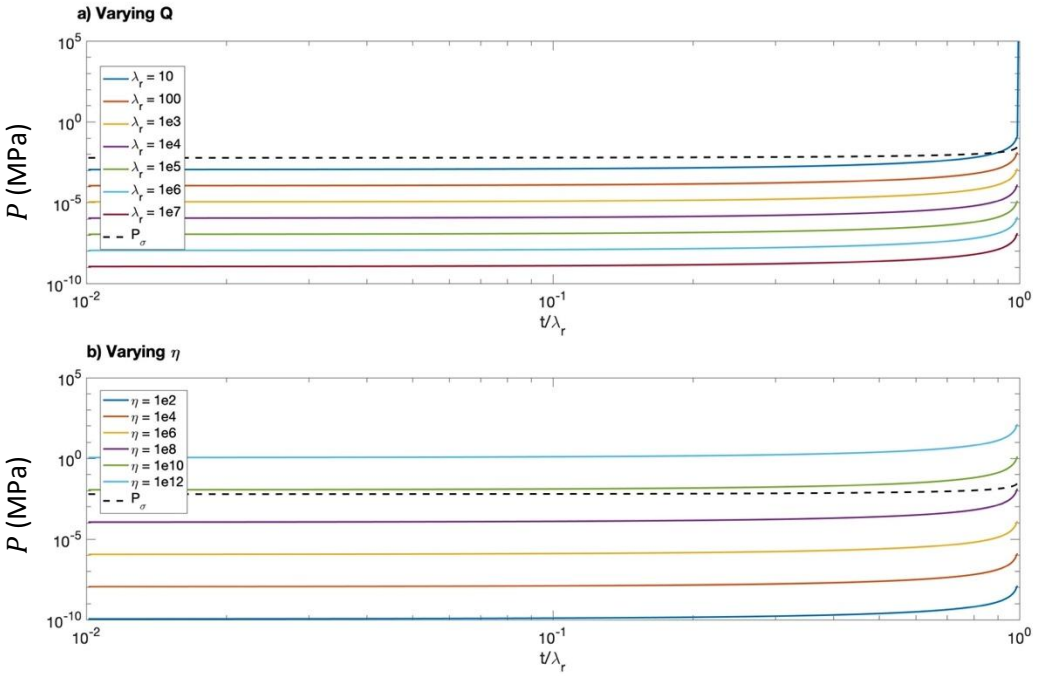

Figure 3.6. Results for the outputs P_η (solid lines) and P_σ (dashed lines) from table 3.2. A) shows the pressure outputs for varying compression timescales under a constant viscosity. B) shows the pressure outputs for varying melt viscosity under a constant compression timescale.

3.6 Adding a dissolved H_2O dependent diffusivity and viscosity calculation

So far, the investigations have assumed diffusivity and viscosity as constant values. But in nature, the physical properties of magma can be highly dynamic with strong dependencies on the conditions at any given time. In this investigation, we incorporate a H_2O dependent diffusivity (Eq. 3.12) and viscosity (Eq. 3.13).

The dynamic diffusivity term is expected to strongly affect the P_g evolution where, over time, the resorption of H_2O is expected to be more efficient as a higher dissolved H_2O concentration increases the diffusivity of H_2O in the melt (Zhang & Ni, 2010). Melt viscosity would decrease over the compression time as H_2O is resorbed back into the melt, this would decrease the viscous resistance from the melt. A dynamic viscosity term is not expected to make a significant contribution to the overall pressure evolution of the magma (as investigated previously). However, it is important for more accurate modelling of natural magma or if one wants to make a follow-up study where viscosity becomes a more important property, for example, if the magma flows following compression.

Dynamic diffusivity and viscosity are investigated under different compression rates whilst keeping all other starting parameters constant. Increasing H_2O concentration from 2-5 wt%, viscosity decreases by 2 orders of magnitude and diffusivity increases by 1 order of magnitude (Figure 3.7). As the viscosity calculation used is also dependent on the melt composition (Eq. 3.13; Giordano et al., 2008), 2 datasets are compiled using 2 different rhyolitic melt compositions: a lower viscosity 'Krafla' and a higher viscosity metaluminous rhyolite. Both have similar anhydrous densities which will be assumed constant for this study. The molecular composition used to calculate the viscosity can be found in the appendix where the compositions are taken from Tuffen and Castro (2009) and *Encyclopedia of volcanoes* (2000) for Krafla and Rhyolite respectively. The parameters investigated are given in the table 3.3:

Table 3.3. Model Parameters to test the effects of dissolved H_2O and dynamic diffusivity during the compression of a bubble cell

Total cell volume (v_c)	1.2e-11
Diffusivity (D)	Variable (Eq. 3.12)
Viscosity (η)	Variable (Eq. 3.13)
Initial Gas volume fraction (ϕ)	0.16
Compression timescale $(\overline{\lambda_r})$	100-10^7s
Volume compression rate (Q)	$\frac{v_c\phi_0}{\overline{\lambda_r}} \approx 1.2\times10^{-14}$ -1.2×10^{-19} (m^3/s)
Initial ambient pressure (P_0)	50MPa
Temperature (T)	1000°C
Melt density (ρ_m)	2426.5 (Kgm^{-3})
Surface tension (σ)	0.22 (Nm^{-1})

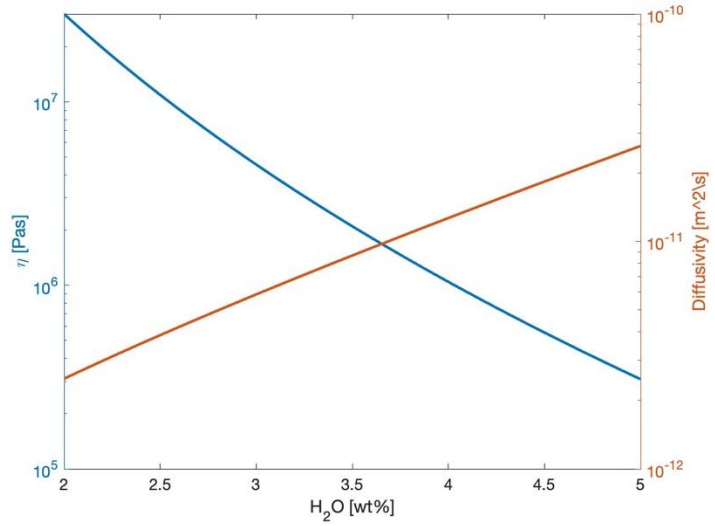

Figure 3.7 In-situ, isothermal, isobaric variability of Viscosity (η) and diffusivity (D) due to dissolved H_2O concentration. Composition is set as 'Krafla' (Tuffen and Castro., 2009). Using the viscosity calculations from Giordano et al. (2008) and the diffusivity calculation by Zhang & Ni (2010).

Additional steps are required for normalisation and analysis due to diffusivity varying not only temporally but spatially over the length of the melt shell. Average diffusivity across the melt shell under spherical Lagrangian coordinates is calculated by equation 3.20. Similarly, viscosity also varies spatially across the melt shell so calculating effective viscosity can be done by replacing $D(A)$ with $\eta(A)$ in equation 3.21:

$$\bar{\eta} = \frac{1}{\frac{4\pi A_f^3}{3} - \frac{4\pi A_0^3}{3}} \int_{A_0}^{A_f} 4\pi A^2 \, D(A) dA = \frac{3}{\left(A_f^3 - A_0^3\right)} \int_{A_0}^{A_f} A^2 \, D(A) dA \qquad \text{(Eq. 3.25)}$$

The results for table 3.3 show that the normalised gas pressure (Eq. 3.23) over normalised time, and Pe plots are negligibly affected by the dynamic diffusivity term (Figure 3.8b & c), producing similar plots and trends to figure 3.4b & d. The Pe plots (Figure 3.8a) also show trends like figure 3.5. The dynamic diffusivity term used is independent of any melt composition dependencies so there are no noticeable variations between the Krafla and Rhyolite plots on figure 3.8. Insignificantly small changes in P_g between melt compositions may be observed due to tiny changes in P_∞ & P_η due to differences in viscosities which would slightly affect the calculation of D, but there is seemingly no difference between the average

diffusivities across the melt between the 2 compositions (Figure 3.9). As the

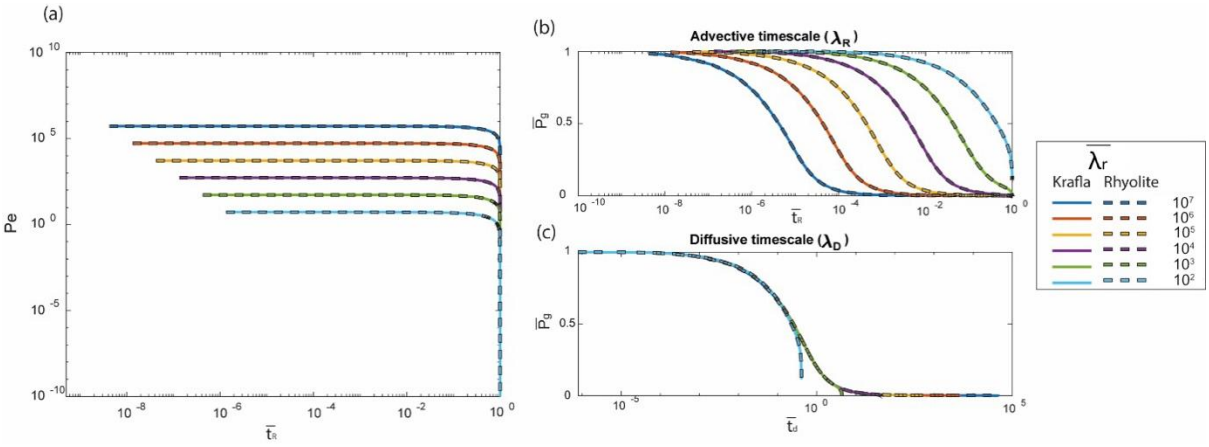

Figure 3.8. Dimensionless results for table 3.3, solid lines and dashed lines represent the two melt compositions used. A) the evolution of Pe over $\overline{t_R}$. B) normalised gas pressure $\overline{P_g}$ over normalised advective time $\overline{t_R}$. C) normalised gas pressure $\overline{P_g}$ over normalised diffusive time $\overline{t_R}$.

diffusivity does not vary due to temperature in an isothermal magma chamber, the plots show that dissolved H_2O concentration is the most important factor in calculating dynamic diffusivity. Compression rates correlating to $Pe \gg 1$ show little difference in diffusivity (Figure 3.9) as $Pe \gg 1$ is associated with equilibrium diffusion. The effective diffusivity range for the equilibrium solution is 1.5-1.8 $\times 10^{-11}$ m^2/s which shows that diffusivity does not vary significantly enough to make a significant impact on the H_2O resorption rate.

For high compression rates (i.e. $\lambda_r \leq 10^3$s) the diffusivities appear to fall off the equilibrium curves and increase at slower rates than equilibrium as H_2O is being resorbed at a slower rate, this produces a negative feedback where the low diffusivity and H_2O resorption are dependent on one another. For extreme cases where $\lambda_r \leq 10^3$s (equivalent to $Pe \leq 1$), the diffusivities show little variation from the initial diffusivity, indicating that resorption cannot keep up with diffusion (Figure 3.9b). Therefore, more H_2O molecules are trapped in the gas and diffusivity does not vary due to an increase in dissolved H_2O concentration. At the end of the low Pe simulations, the diffusivity decreases significantly. This indicates that P_∞ is approaching infinity due to P_σ increasing at small bubble radii. The rapid pressure increase subsequently reduces the diffusivity towards zero as diffusivity is partially dependent on pressure (Figure 3.9).

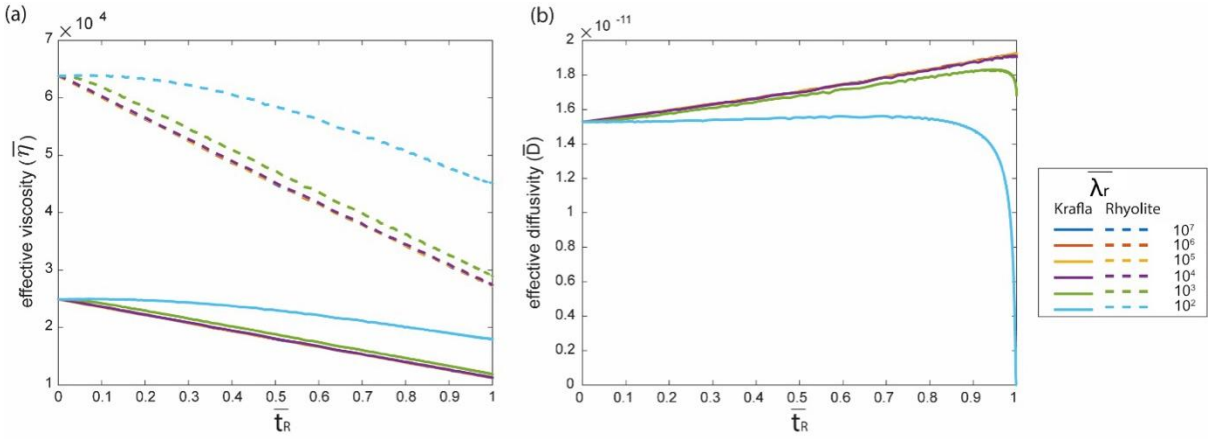

Figure 3.9. A) Evolution of effective viscosity $\bar{\eta}$ [Pas] (equation 3.24) over normalised time for two melt compositions from table 3.3. B) Evolution of effective viscosity $\bar{D}$[m²/s] (equation 3.20) over normalised time, there is no variability in diffusivity between the 2 melt compositions.

Viscosity on the other hand does vary noticeably due to composition where 2 distinct 'clusters' of trends appear on the effective viscosity results (Figure 3.9a), both clusters show similar trends to one another. Similar to diffusivity, at compression rates associated with $Pe \gg 1$ (λ_r = $10^{3\text{-}7}$s), the H_2O resorption is at equilibrium, so concentration dependent viscosity is shown to be at equilibrium. At lower Pe values, the viscosity profiles stray from the equilibrium trend as less H_2O is being resorbed. Rhyolitic magma is generally more viscous than Krafla magma due to the higher SiO_2 content which is shown on the viscosity graph where the rhyolite curve cluster is higher than the Krafla cluster. Higher SiO_2 also makes viscosity more sensitive to dissolved H_2O concentration which explains why the viscosity over time gradient of Rhyolite is greater than Krafla even though the H_2O resorption isn't varying between the two compositions. These viscosity variations however, would not produce any meaningful changes to P_η as the viscosities range between 1-8 $\times 10^4$MPa, compared with the P_η plots on figure 3.10 ranging from $\sim 10^{-9}$-10^{-3} MPa which are negligible and significantly less than P_σ.

While using a dynamic diffusivity and viscosity in the calculations may not produce significant changes to the pressure of the system, it is valuable for more accurate modelling of magma. Using dynamic diffusivity and viscosity terms would calculate diffusivity and viscosity as products of the magma's physical properties rather than making assumptions of D & η. Furthermore, at the fastest compression timescales, the P_η evolution profiles (Figure 9a) break the trend of the slower compression timescales and shows the profiles 'levelling off' by the end of the compression time. The cause of this effect is currently unknown, but it

is suspected that it is due to numerical instabilities from the H_2O concentration by the bubble wall exceeding 100%, causing the viscosity calculation to be unstable.

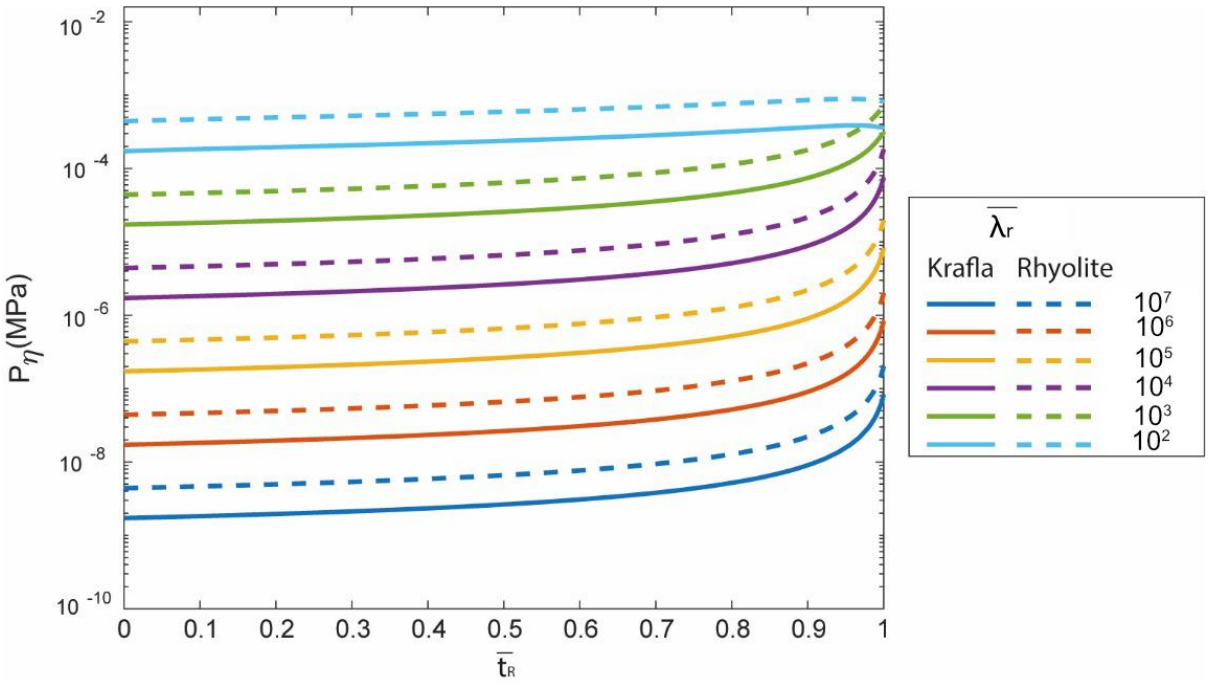

Figure 3.10. Dynamic evolution of P_η over time normalised time for the two melt compositions (table 3.3). This considers spatially dependent melt viscosity across the melt shell in the calculation of P_η (equation 3.6)

3.7 Limitations of the spherical bubble model

This chapter has discussed and shown the benefits of using the spherical bubble lattice model to calculate the pressure evolution of bubbly magma by modelling a 1D profile of a spherical bubble cell. The key limitation to this approach is that it assumes perfect spherical symmetry and uniform forces acting around the bubble cell. Bubbles in magma are not always perfectly spherical and stresses are not likely to be applied uniformly around the bubble cell to retain spherical geometry. For example, if we apply longitudinal forces upon bubbly magma, deformation of the bubble cells may result in a flattened sphere shape along the longitudinal axis, particularly for larger bubbles. However, the tiny bubble volumes modelled in this study are likely to retain spherical shapes due to high surface tension.

Another limitation is that this model assumes that all bubble cells in the lattice uniformly respond to compressional forces and no coalescence of bubbles occur. In order to get the most accurate representation of magma processes, would require fully resolving 3D modelling of bubble cells. Jumping to 3D greatly increases the computational cost of

models. This becomes unfeasible when resolving the dynamics and interactions of all bubbles suspended in a package of magma.

3.8 Discussion and conclusions

This chapter has demonstrated that a Pe number can be a useful tool for predicting the pressure evolution of a bubble in a melt shell under the constraints of a constant volume compression rate. The hydrodynamic equation (equations 3.1, 3.7, 3.8) where P_∞ is a sum of P_g, P_σ & P_η, is dominantly controlled by P_g. Even at extreme values of η & λ_r, the resulting P_η is negligible and almost never exceeds P_σ, P_g, or even beyond 1MPa. Surface tension (P_σ) is also negligible unless at extremely low bubble radii where the P_σ increases towards infinity. This effect in nature would reflect a bubble spontaneously disappearing when the bubble reaches small radii. With these thoughts in mind, one can reasonably assume that the pressure of a gas-liquid system P_∞ is closely reflected by the gas pressure P_g. However, this chapter has also found that it is rare for gas resorption to be in the disequilibrium or transitional pressure evolution regimes $(Pe \leq 1)$. This is shown on figures 3.5 and 3.8, where extremely fast compression timescales $(\lambda_r < 1000s)$ or extremely long diffusive timescales due to low diffusivity are required. A fast compression timescale is unlikely for magmatic systems as magma reservoirs recharge over much longer, geologic timescales. For the case of low diffusivities, for metaluminous rhyolites, one requires lower temperatures, pressures and total H_2O concentrations to produce the low diffusivities required. With these results in mind, it may be a reasonable to conclude that the gas pressure evolution for most compressing magmatic systems occurs at equilibrium with the solubility. Therefore, the full numerical solution (solution 3) may not be necessary for the calculations of pressure of magmatic systems, rather the solubility analytical end-member regime may be sufficient. This drastically reduces the computational time required to calculate the pressure with a known volume change.

However, so far we have only focused on a limited range of initial volume conditions. If the initial bubble radii, melt volumes, or total H_2O concentrations were to be larger or smaller, the results may be different (i.e. when a bubbly magma is approximated into lower bubble number densities). For example, a smaller initial bubble radius would make P_σ start at a greater initial value; greater melt volumes (lower bubble number densities) would increase

the thickness of the melt shell surrounding the bubble, making the P_η greater; higher total H_2O concentrations would make the overall pressures greater and the viscosities lower. The next chapter will upscale the 'bubble cell' model to reflect the conditions and geometries of a bubbly magma reservoir, testing natural parameters and different initial conditions to see how the pressure of a natural magma chamber would evolve and what limits are required to push natural systems into disequilibrium.

4 – Pressure evolution during the recharge of a bubbly magma reservoir

4.1 Introduction

This chapter synthesises the findings of the previous chapters and applies the models to natural scenarios; hence, the title of this chapter shares the title of the thesis. In the previous chapters, a method of numerically calculating the pressure evolution of a gas-liquid system under a known volume compression rate was presented. The model adopts the 'bubble cell' model by Prousevitch et al., (1993b), consisting of a bubble surrounded by a shell of incompressible melt; the model is modified to output the pressure (P_∞) under an input gas volume change (ΔV). The previous studies focused on the dynamics of a single bubble surrounded in melt, the main findings of the previous parametric studies so far are:

- Diffusion of H_2O through the melt is the most significant factor in determining the pressure evolution. The number of H_2O molecules left undissolved in the gas phase determines the gas pressure of the bubbles in the magma $\left(P_g\right)$.
- A Peclet number (Pe) is a dimensionless number that characterises which pressure regime a compressing bubble follows: Diffusive equilibrium regime $(Pe \gg 1)$, transitional regime $(Pe \sim 1)$ or the no diffusive flux regime $(Pe \ll 1)$.
- Viscous resistance $\left(P_\eta\right)$ is a relatively insignificant factor for the pressure calculations unless at extremely high melt viscosities or compression rates.
- The difference between gas pressure $\left(P_g\right)$ and magma pressure (P_∞) is largely dependent on the surface tension (P_σ) which has an increasingly significant effect as the magma bubbles get smaller.

It was found that Pe was generally in the equilibrium regime, except in extreme circumstances such as fast compression rates where the compression timescale is much shorter than to the diffusion timescale $(\lambda_R < \lambda_D)$. The previous chapter found that for a total cell volume $(v_C = v_g + v_m)$ ~1.2×10^{-11}m^3 with an initial gas fraction of 0.16, extremely fast compression where compression timescales λ_R<100s, are required for Pe to reach the transitional regime. In this chapter, the numerical model introduced in the previous chapter

will be tested using natural scenarios and parameters to test whether or not all natural scenarios of bubbly magma under compression would compress slow enough for the diffusion and gas pressure to fall within the equilibrium solution. If all magma reservoirs do compress at equilibrium, the equilibrium end-member solution is feasible for modelling the pressure evolution in all scenarios similar to equations 2.4 and 3.9:

$$P_{gE}(t) = \frac{8.314 n_g(P_{gE}, t) T}{v_g(t)} \quad \text{(Eq. 4.1)}$$

Where n_g is calculated at equilibrium at gas pressure P_{gE} and temperature T. The implicit solution on equation 4.1 gives accurate calculations of P_g under a known volume compression based on the physical properties of the magma. Consequently, if the equilibrium regime can be assumed for all bubbly systems, the simple assumptions for magma compressibility β_m by Huppert and Woods (2002) based on H_2O concentration and magma depth can be used where volume can be calculated based on the pressure applied onto the compressible magma:

$$\frac{1}{\beta_m} = \frac{1}{\beta_r} + \frac{1}{\rho}\frac{\partial \rho}{\partial P} \quad \text{(Eq. 4.2)}$$

Where β_r is the wall rock compressibility and ρ is the magma density as a function of melt, gas and crystal densities in the magma. The results from this investigation may improve modelling of magma bodies by recommending the appropriate method of calculating pressure evolution in a bubbly magma reservoir. The previous examples from the previous chapters modelled the processes on a single gas-liquid system. To test for a whole magma body, we adapt the setup parameters to be representative of the whole magma body rather than for a single bubble cell.

4.2 Methods and model setup

I illustrate a “bubbly magma reservoir” as a subsurface region of melt and gas. Solid crystals and thermal effects are omitted for simplicity in order to model the end-member scenario of a pure isothermal gas-liquid magma. Magma is hosted in a single subsurface cavity with

total volume V_C; initially, the magma consists of an incompressible liquid melt and gas bubbles with their sums equal to the total cavity volume:

$$V_C = V_m + V_{g0}$$

Or in terms of initial gas fraction:

$$V_C = (1 - \phi_0)V_C + \phi_0 V_C$$
$$V_m = (1 - \phi_0)V_C$$
$$V_{g0} = \phi_0 V_C$$

Where the first and second terms on the right-hand side of the above equation equalling V_m & V_{g0} respectively. As no elastic response from the cavity walls is assumed, and the gas bubbles are the only compressible phase, when the magma reservoir is subject to a constant magma recharge rate Q (note Q is distinct from Q_c from the previous chapter where the previous chapter focused on the compression of a single bubble), the injected volume is completely accommodated by a reduction in the gas volume. We also assume the new injected magma to be incompressible and does not mix with the pre-existing magma, so compression caused by the magma recharge acts as a 'piston' (Figure 4.1). This yields the volume balance:

$$V_C = V_m + V_{g0} - Qt \qquad \text{(Eq. 4.3)}$$

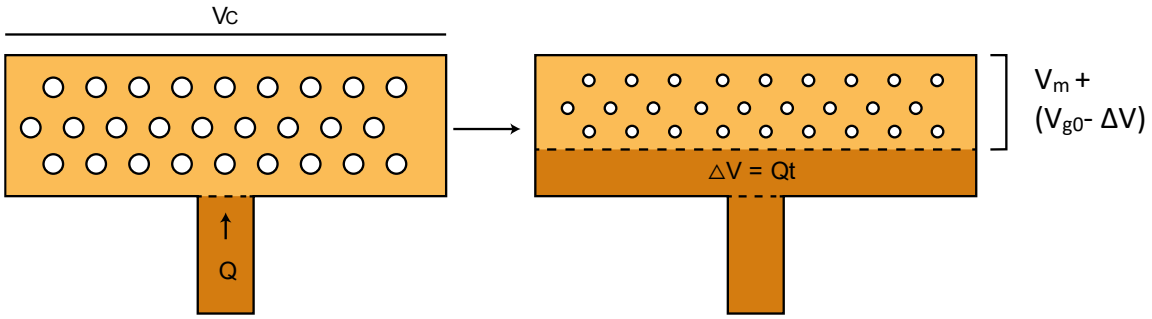

Figure 4.1. Schematic illustration of the "piston compression" model of a magma chamber. Total rigid magma reservoir volume V_C is constant and the sum of the initial gas volume V_{g0} and incompressible melt volume V_m. The pre-existing magma body is homogenously compressed by a constant magma influx Q to a total volume change $\Delta V = Qt$. Elastic response from the chamber walls, magma mixing, and thermal effects are omitted.

The models from the previous chapters have assumed the compression of a single bubble surrounded by a melt. For this model we upscale the 'bubble cell' model to reflect a whole magma body. The pre-existing magma in figure 4.1 is approximated into a lattice of bubble cells with a bubble number density of N_b per m^3, all the bubble cells in the lattice are

identical and deform homogenously. We repeat the 'bubble cell' model of the previous chapter in order to model the pressure evolution of an entire magma reservoir by 1-D modelling of a single bubble cell in the lattice. This is illustrated in figure 4.2 which is repeated from the previous chapter.

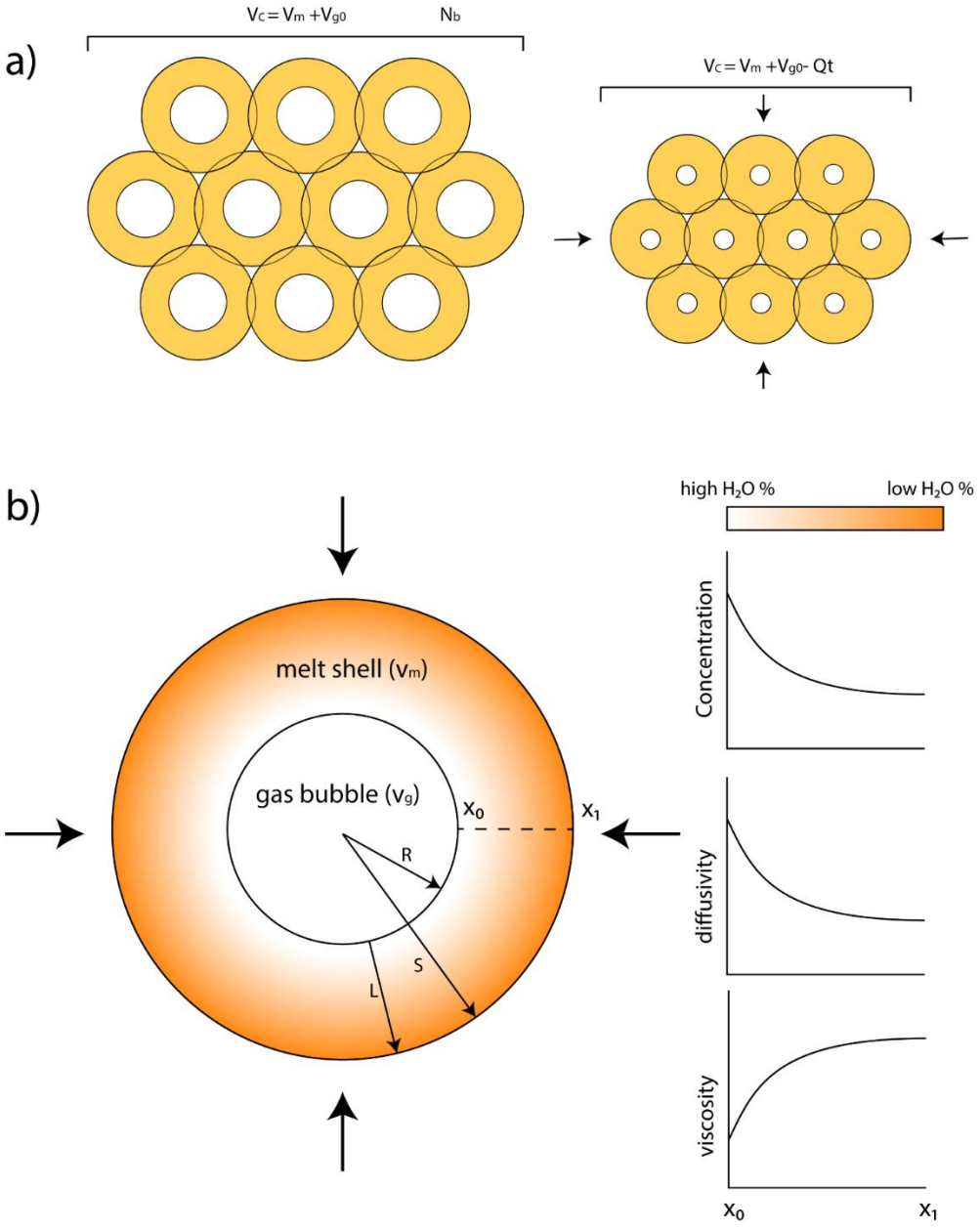

Figure 4.2. Repeated figure 3.1 as it is still important for this chapter. a) Illustrating the approximation of the bubbly magma into the bubble cell lattice. Uppercase V_C, V_m & V_{g0} are the total chamber, incompressible melt, and initial gas volume respectively, Qt is the compression rate or magma influx rate multiplied by time, the same as figure 4.1. b) schematic of an individual bubble modelled in the lattice, the associated dimensions and the expected profiles of concentration-dependent diffusivity and viscosity. Lowercase v_m& v_g are the melt and gas volumes of the bubble cell. S & R are the radius of the total cell and gas bubble. L is the thickness of the melt shell and lagrangian coordinates across the melt shell are constrained between x_0(bubble-melt interface) and x_1(edge of the total cell)

If all the bubbles in the lattice are assumed to compress homogenously, the volume of the single bubble in the lattice (v_g) equals:

$$v_g = \frac{V_{g0} - Qt}{V_m N_b} \quad \text{(Eq. 4.4a)}$$

Note that $V_{g0} = V_c\phi_0$ and $V_m = V_c(1-\phi_0)$ (Eq. 4.3), hence

$$v_g(t) = \frac{V_c\phi_0 - Qt}{V_c(1-\phi_0)N_b} \quad \text{(Eq. 4.4b)}$$

which expresses $v_g(t)$ in terms of input parameters. Thus bubble radius can be expressed as:

$$R = \left(\frac{3}{4\pi}\frac{V_c\phi_0 - Qt}{V_c(1-\phi_0)N_b}\right)^{\frac{1}{3}} \quad \text{(Eq. 4.4c)}$$

Assuming the bubble is a perfect sphere throughout. Thus, the radial compression rate $\dot{R}$ $\left(or\ \frac{dR}{dt}\right)$ for a single bubble can be solved analytically when differentiating R with respect to time:

$$\frac{dR}{dt} = \dot{R} = -Q\left(\frac{1}{36\pi V_c(1-\phi_0)N_b(V_c\phi_0 - Qt)^2}\right)^{\frac{1}{3}} \quad \text{(Eq. 4.5)}$$

Note that the above equations are only valid for a constant Q. If we assume the new magma does not mix with the pre-existing magma, Q will act as a 'piston' from the bottom of the chamber that reduces the gas volume ΔV driven by an increasing ambient pressure P_∞. Equations 4.4 a, b, c and 4.5 allow the numerical setup established in the previous chapter (equations 3.6and 3.17) to be set up in terms of the chamber parameters rather than bubble parameters.

4.3 Adjustments to analysis

As the volume relationships in this chapter now reflect the volumes of a whole magma body rather than on an individual bubble scale, adjustments are made to the calculation of Pe and the associated timescales of the system. The compressive timescale as a function of the chamber parameters is given as:

$$\lambda_R = \frac{V_C \phi_0}{Q} \quad \text{(Eq. 4.6)}$$

Which gives a linear normalised advective time:

$$\bar{t}_R = \frac{t}{\lambda_R} = \frac{tQ}{V_C \phi_0} \quad \text{(Eq. 4.7)}$$

The diffusive timescale is dependent on the spatial variability of H_2O diffusivity across the melt shells on the bubble scale so the methods for calculating λ_D & $\bar{t}_D$ are the same as the previous chapter (equations 3.21 and 3.22). In equation 4.8, the calculation of Pe is reiterated from the previous chapter as it remains a central theme of this chapter to define the pressure regime of naturally scaled magma chambers.

$$Pe = \frac{\lambda_R}{\lambda_D} = \frac{R\bar{D}}{\dot{R}L^2} \quad \text{(Eq. 4.8)}$$

Where λ_R is a dynamic compressive timescale based on the radial evolution of each bubble in the lattice, separate from the linear chamber compressive timescale given in equation 4.6)

4.4 Large vs small magma reservoirs

Here, I define 2 categories for magma chamber volume to test the effects of chamber geometry and recharge rate. These categories are used to compare a) a single reasonable estimate for a large, caldera-type, shallow magma reservoir volume under variable recharge rates and b) a range of magma chamber volumes from small to large, representing volumes for small sill/dyke type intrusions under a constant recharge rate (Table 4.1). Crystal-poor magma reservoirs beneath caldera complexes are estimated to be mostly in the order of magnitude of 10km^3 (e.g. Krafla ~ 30km^3 (Einarsson, 1978; Brandsdóttir and Menke, 1992; Schuler *et al.*, 2015), Laguna del Maule ~ 20Km^3 (Le Mével, Gregg and Feigl, 2016)), which will be the estimate for a V_C for a natural magma reservoir. For the lower volume end-member simulations, V_C is chosen as 1000m^3. Such a small volume may be representative of a small dyke containing bubbly magma or a localised pocket of crystal-poor magma within a mush. Both volumes tested assume a perfectly isothermal system in a perfectly rigid confining rock and compressed over the timescale λ_R equating to a constant magma

recharge rate $Q = \frac{V_C \phi_0}{Q}$. The models are started with a gas volume fraction ϕ_0 of 0.16 at equilibrium with the initial pressure, ϕ_0 is calculated as the equilibrium volume of a 3wt% H_2O magma rising from saturation depth to P_0 using the H_2O solubility function(Eq. 3.11).

We test a range of magma recharge timescales from reasonable geological constraints to more unrealistic, extreme cases in order to pinpoint which conditions are required for the pressure to evolve in disequilibrium with solubility $(Pe \leq 1)$. The estimated range of filling rates for tabular granitic plutons is between 0.01-100m^3/s (Petford et al., 2000). While it is possible that greater injection rates may occur, Q = 100 m^3/s will be used as a geological constraint for the maximum natural injection rate. Higher compression rate where $Q \gg$ 100m^3/s will also be modelled to identify what compression rates are required to deviate from the equilibrium regime for a natural magma chamber (Table 4.1a). I also investigate the effects of varying reservoir volume, smaller magma reservoirs would have a smaller total gas volume to occupy. I test a range of V_C values <10km^3 with a constant Q = 100 m^3/s to see whether the geological constraint on magma injection rate can produce disequilibrium pressure evolution for smaller magma bodies (Table 4.1b).

Table 4.1 Model Parameters for magma reservoirs under compression, exploring variable recharge rates and different magma reservoir sizes.

	(a) Caldera-type natural analogue volume, variable recharge rates	(b) variable volume magma reservoir under constant recharge rate
Chamber Volume (V_C)	10km^3	10^4 - 10^{10}m3
Volume influx rate (Q)	10^2-10^8m^3/s	100m^3/s
Initial Gas volume fraction (ϕ)	0.16	0.16
Bubble number density (N_b)	1×10^{12} bubbles /m^3	1×10^{12} bubbles /m^3
Initial ambient pressure (P_0)	50MPa	50MPa
Temperature (T)	1000°C	1000°C
Melt density (ρ_m)	2500 (Kg/m^3)	2500 (Kg/m^3)
Surface tension (σ)	0.22 (N/m)	0.22 (N/m)

Melt composition (wt%) Giordano et al., (2008)

SiO_2	TiO_2	Al_2O_3	FeO	MnO	MgO	CaO	Na_2O	K_2O	P_2O_5	H_2O	F_2O-1
76.38	0.06	11.59	1.03	0.05	0.36	3.25	2.44	4.66	0	Variable	0

4.4.1 Table 4.1a results – Large magma bodies

The conditions listed in table 4.1a & b both start the model with initial volumes at t_0 of a single bubble ~1.2×10^{-13} m^3 surrounded by a melt volume of 1×10^{-12} m^3. In table 4.1a, the tested magma volume recharge rates 10^2-10^8m^3/s equates to relative recharge timescales (λ_R) ranging between 1.6×10^7 - 16s (or ~0.5 years - 16s) given the maximum injected volume is 1.6Km^3 $\left(\lambda_R = \frac{\phi_0 V_C}{Q}\right)$. The outputs P_g & P_∞ do not vary significantly from one another, the difference between P_g & P_∞ is dominantly controlled by P_σ, where $P_g > P_\sigma$ as the $-P_\eta$ profile is consistently at least 6 orders of magnitude below P_σ (Figure 4.3b & c). The P_g profile follows the equilibrium end-member solution, this is shown as the dissolved H_2O concentration profile over time which is uniform throughout time, following the equilibrium solubility (Figure 4.3d).

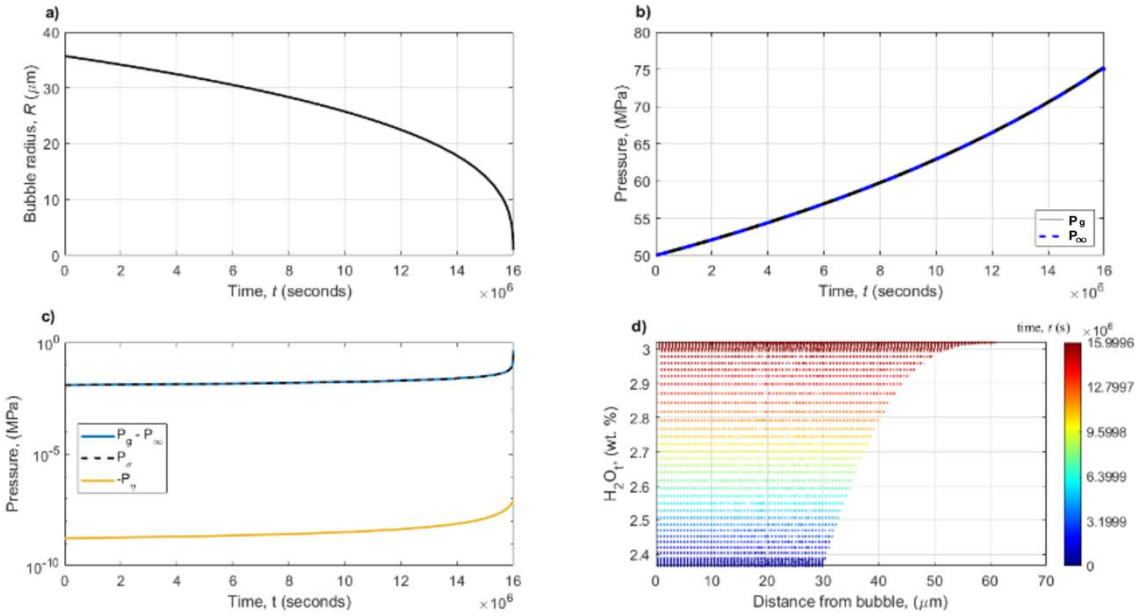

Figure 4.3. Dimensional results for ***Error! Reference source not found.****a, for* $Q = 100m^3s^{-1}$*, reflecting the upper limit of estimated magma injection rates. a) bubble radius over time (equation 3.3). b)* P_g *&* P_∞ *over time,* P_g *follows the same profile as the equilibrium end-member solution consistently. c) The evolution of* $P_g - P_\infty, P_\sigma$ *&* $-P_\eta$ *over time. d) dissolved volatile concentration profile across the melt shell over time. Consistent uniform profiles from bubble wall to the shell edge shows that diffusion occurs fast enough to be at equilibrium with compression.*

For the parameters listed in table 4.1a, Q rates up to 10^5m^3/s (λ_R=16000s) also follow the equilibrium end-member., these correlate with a Pe profile consistently greater than 1 (Figures 4.4a & b). When Q=10^6m^3/s (λ_R = 1600s), the pressure evolution follows the equilibrium solution throughout most of the simulation time but lifts off from equilibrium near the end of the simulation time. This is because the Pe profile starts at the equilibrium regime $(Pe \gg 1)$ but falls towards the transitional regime $(Pe{\sim}1)$ at small bubble radii, indicating that the H_2O diffusion through the melt cannot keep up with the volumetric compression. Q = 10^7m^3/s shows a Pe profile starting at the transitional regime and decreasing over time. This produces a P_g profile with a more significant pressure difference from equilibrium and increasing further as Pe decreases further below 1. The extreme case of Q=10^8 m^3/s correlates with a Pe profile consistently below 1, producing a P_g profile leaning closer to the no diffusive flux end-ember solution.

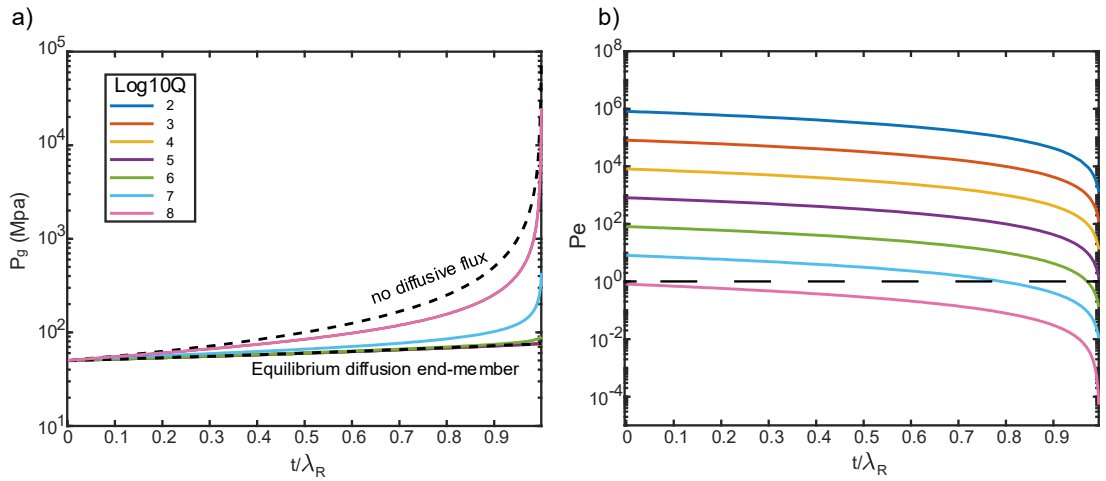

Figure 4.4 a) Evolution of gas pressure plotted against normalised time, dashed black lines are the no diffusive flux and Equilibrium diffusion end member solutions. b) Pe plotted against normalised time, black dashed line shows $Pe = 1$ which separates the equilibrium and no diffusion regimes.

4.4.2 Table 4.1b results – Small magma bodies under variable magma influx rate

Smaller magma bodies of the same physical properties as table 4.1a would maintain the same gas fractions but due to the smaller initial volumes, would contain a smaller gas volume. Table 4.1b lists parameters to test whether the geological constraint for magma injection rate (Q = 100m^3/s) can cause disequilibrium for smaller magma bodies. Figure 4.5show similar trends as Figure 4.4 for both the P_g & Pe evolution. Larger V_C simulations ($V_C > 1 \times 10^6 m^3$) show P_g profiles following the equilibrium pressure regime and consistently high Pe due to a high λ_R compared with λ_D. In the previous chapter, it was found that while the diffusivity of H_2O in the melt increases due to dissolved H_2O concentration, $\overline{D}$ & λ_D does not vary significantly to affect the Pe. The Pe is largely dependent on λ_r $\left(\frac{R}{\dot{R}}\right)$ which becomes shorter at smaller V_C as the lower gas volume is compressed in a shorter time due to a contant Q (Figure 4.5). The faster $\frac{dR}{dt}$ ($\dot{R}$) for smaller magma bodies also causes the P_η to increase and the profiles shifts upwards proportionately with smaller V_C. At the lowest V_C, the anomalous P_η profile that doesn't show a power-law increasing P_η trend as the other profiles at higher V_C (similar to what was observed in figure 3.10 at high compression rates), while the exact cause of this observation is unknown, it is speculated that the Giordano viscosity calculation is unstable at low Pe where the H_2O concentration at the boundary condition reaches close to 100 wt% H_2O, this makes

calculating P_η numerically unstable. However, all the -P_η profiles remain consistently below P_σ meaning P_η remains a negligible quantity (Figure 4.6).

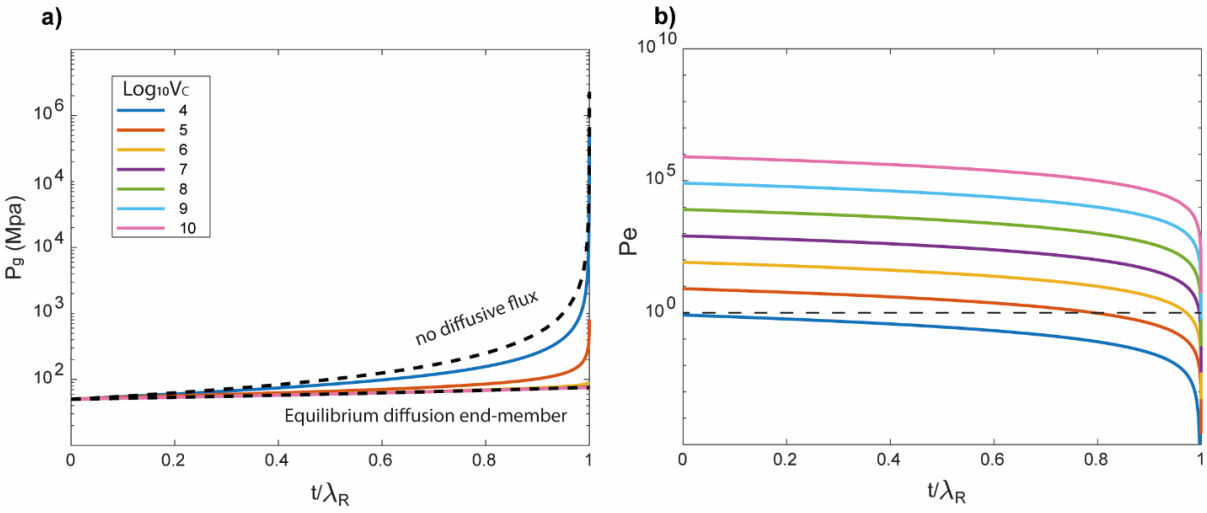

Figure 4.5 a) Evolution of gas pressure plotted against normalised time, dashed black lines are the no diffusive flux and Equilibrium diffusion end member solutions. b) Pe plotted against normalised time, black dashed line shows $Pe = 1$ which separates the equilibrium and no diffusion regimes.

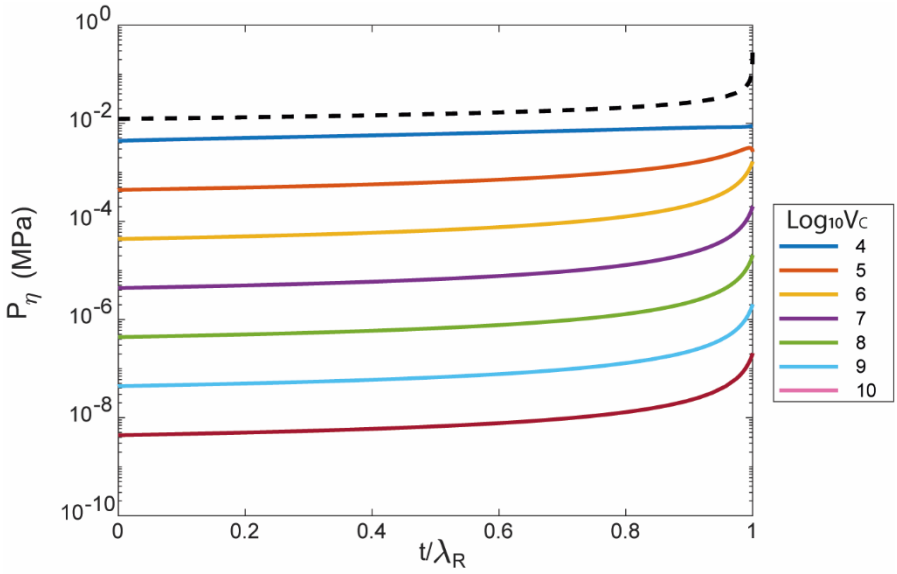

Figure 4.6 Viscous resistance evolution over normalised compression time for different chamber volumes. Black dashed line is P_σ

4.4.3 Effects of bubble number density/bubble distribution

So far I have approximated the bubbles into a constant lattice of 10^{12} bubbles/m^3 of melt. However, if we approximate the bubble lattice into smaller or higher N_b values, this would affect both the advective and diffusive timescales as N_b is linked with the dimensions of the bubble cells (equations 4.4a, b, c and 4.5) For example, if we approximate the same gas

fraction into a higher N_b, the volume of each bubble cell is lower and so we expect the pressures in the bubble to evolve at equilibrium more easily due to higher Pe profiles, and the effect of P_η would be more negligible as the shell thickness L is thinner and $\frac{dR}{dt}$ would be smaller. P_σ is expected to make up a greater portion of the output P_∞ as the bubble cells have smaller initial radii. (Note that the overall gas volume in the chamber remains constant in these scenarios, just approximated into more bubble cells). However, having a smaller N_b approximates the bubble cells into larger, more spaced-out bubbles which may cause disequilibrium, mainly due to a longer diffusive timescale associated with a thicker melt shell. The table below lists parameters to test the effects of N_b on the output pressure. The geological constraint of $Q = 100$ is used again in this investigation under the same V_C & ϕ_0 for each N_b tested. I set V_C as the natural estimate of a crystal-poor magma body at 10km^3, the same as table 4.1a.

Table 4.2. Model Parameters for a magma chamber under compression, but with variable bubble distribution densities.

	Variable N_b										
Chamber Volume (V_C)	10km^3										
Volume influx rate (Q)	100m^3/s										
Initial Gas volume fraction (ϕ)	0.16										
Bubble number density (N_b)	10^8-10^{15} m^{-3} (& 10^3 m^{-3})										
Initial ambient pressure (P_0)	50MPa										
Temperature (T)	1000°C										
Melt density (ρ_m)	2500 (Kg/m^3)										
Surface tension (σ)	0.22 (N/m)										
Melt composition (wt%) Giordanoet al., (2008)											
SiO_2	TiO_2	Al_2O_3	FeO	MnO	MgO	CaO	Na_2O	K_2O	P_2O_5	H_2O	F_2O-1
76.38	0.06	11.59	1.03	0.05	0.36	3.25	2.44	4.66	0	Variable	0

The results for table 4.2 shows that varying N_b also produces predictable profiles for Pe that shifts up or down due to higher and lower N_b respectively (Figure 4.7a), each Pe profile has the same shapes seen in figure 4.4b & figure 4.5b. However, for the given parameters set in

table 4.2, the Pe profiles produced fall well within the equilibrium diffusion regime, the threshold for the Pe profiles to start below 1 is at $N_b = 10^3$ (dashed black line, figure 4.7a). Figure 4.7b shows that the effects of P_σ increases proportionately with N_b, where at higher N_b the initial bubble radii is smaller, producing a higher initial P_σ. Viscosity does not spatially throughout the tested N_b values, this is because the diffusive regime is firmly in the equilibrium regime for a wide range of N_b, This produces the same P_η profiles for all N_b values as the bubble cell dimensions and $\frac{dR}{dt}$ that affect the calculation of P_η scale proportionately with N_b.

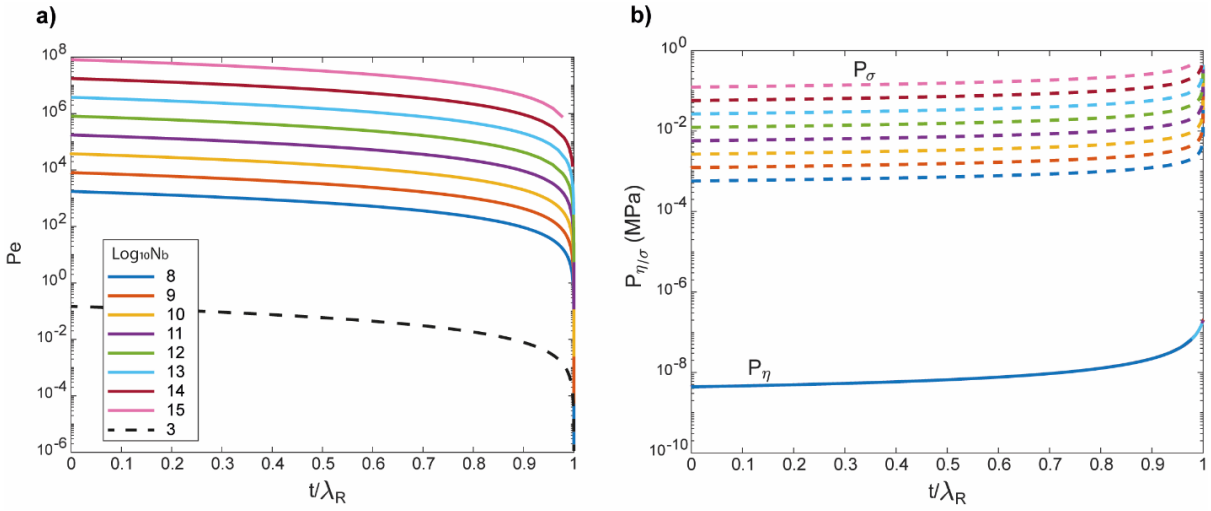

Figure 4.7 a) The Pe evolution profiles as the magma is being compressed for varying N_b. b) The profiles of P_η (solid lines) and P_σ (dashed lines) throughout the compression time.

4.5 The case for a decoupled gas layer overlying melt

So far, we have assumed that bubbles in a magma reservoir can be approximated into a lattice of bubbles suspended in melt, this is a reasonable assumption considering the high viscosity of silicic magmas means the bubbles do not have sufficient buoyancy to rise to the top of a magma reservoir and so get trapped in suspension. However, if the melt has low viscosity, or if the magma reservoir is sufficiently long-lived, an accumulation of gas may exist as a separate layer on the top of the magma reservoir rather than as a suspension of bubbles. In this case, the bubble cell model cannot be used to calculate the pressure evolution during a magma recharge event as there are no bubbles suspended in the melt. However, for this case the cylindrical model from 2 may be used, where the magma reservoir is approximated into a squashed cylinder geometry and the piston arm is

substituted by the injected new magma (Figure 4.8). Here we can repeat the numerical setup described by equations 2.2 and 20 to model the gas pressure evolution.

While modelling of this scenario has not been produced for this study, below, we discuss predictions of magma chamber evolution for a decoupled gas-liquid magma chamber under compression. We base these predictions on Pe analysis done throughout this thesis, applying the geometry similar to chapter 2.

If we take the same volumes and gas proportions as table 4.1omitting N_b, we start with an initial chamber, melt and gas volumes (V_C, V_m & V_{g0}) of 10km^3, 8.4km^3 & 1.6km^3 respectively. Assuming a constant diffusivity of 2×10^{-11}m^{2}s^{-1} (rounded from equations 2.6 and 3.12), with 2.7% H_2O, 50MPa & 1273.15K), assuming the gas melt interface has a cross sectional area of 10km^{2}and a total reservoir thickness of 1Km; at a magma recharge rate of Q=100m^{3}s^{-1}, the average Pe number is calculated at Pe = 3.2×10^{-10}. This is an extremely low Pe number which is dramatically in the no diffusive-flux end-member regime where the gas resorption rate is much slower than the gas compression rate as the specific surface area for gas resorption is significantly smaller without bubbles. Therefore, for the assumption that a separate gas layer exists on the top of magma reservoirs, we predict that the pressure would evolve in disequilibrium with solubility; thus requiring a full numerical solution to calculate the gas pressure evolution, or more simply calculated according to the end-member solution 1 if resorption is considered too slow a full set of models and parameter sweeping must be produced in order to validate the prediction. This also omits the viscous resistance from the underlying melt (P_η) which we would expect to play a much greater role as the underlying melt has a significantly greater thickness than a melt shell surrounding a bubble, but still relatively insignificant given the tiny values shown for P_η previously.

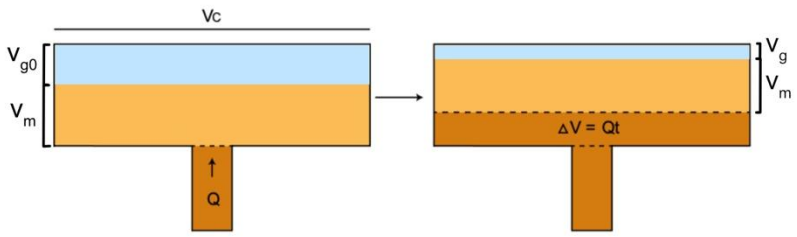

Figure 4.8 Schematic illustration of a squashed-cylinder shaped magma reservoir with a gas layer at the top of a magma reservoir. The new magma injection Q acts as a "piston arm".

4.6 Discussion

The geological constraints I tested in this chapter (excluding the separate gas layer scenario) are not sufficient for Pe to be in the disequilibrium or transitional Pe regime. Ultimately, this is due to the timescales associated with compressing a magma chamber. In order to push the system into pressure disequilibrium, the compressive timescales (λ_R / λ_r) needs to be minimised while the diffusive timescales (λ_D) need to be maximised. Below the calculation of Pe and λ_R are repeated for clarity:

$$Pe = \frac{\lambda_r}{\lambda_D} = \frac{R\bar{D}}{\dot{R}L^2}$$

$$\lambda_R = \frac{V_C \phi_0}{Q}$$

In this chapter, we find that chamber-scaled dimensions need to be pushed to extreme values to push Pe into disequilibrium. For example, the compression timescales can be minimised by pushing the injection rate beyond the geological constraint of 100m^3s^{-1} and injecting into smaller magma bodies. While higher injection rates greater than 100m^3s^{-1} are possible, high injection rates are unlikely to be sustained for long periods of time. Models calculating magma volume injection rates into a long-lived reservoir calculate volume flux as a function of the pressure difference between the injection source and sink (e.g. Le Mével et al., (2016)). As magma is injected, the sink of the injection (i.e. the long-lived magma body) increases pressure which causes the magma injection rate to decrease over time. The diffusive timescales can be maximised by having a lower bubble number density which approximates melt shells surrounding bubbles being much smaller. In the previous chapter, it was established that the chemical diffusivity of H_2O ($\bar{D}$) dependent on dissolved H_2O concentration itself does not vary significantly enough to affect λ_D, but melt shell thickness

can vary over orders of magnitude relative to the bubble number density. Combining high compression rates, low magma volume and low N_b may push Pe closer to the disequilibrium regimes but geological constraints make this highly unlikely. We have focussed on a magma reservoir at 50MPa depth, but if we consider even shallower magma reservoirs where the total H_2O concentration (dissolved + exsolved ~3wt%), the initial gas fraction would start at a higher value as the initial solubility is lower. In this case Pe may yet be even greater as λ_R is greater at the same geological constraint of magma recharge rate Q. Smaller initial bubbles may make the system edge closer to disequilibrium as seen in figure 4.7, but small bubbles are more unlikely to remain stable when suspended in melt due to the higher surface tension driving small bubbles to spontaneously shrink and disappear.

Other factors that affect pressure may force the system into disequilibrium. For example, seismic excitation may cause pressure to fluctuate slightly. Seismic disturbance of the system may occur from external sources such as an earthquake or could be internally generated within the magma. The magnitude of seismic P-wave disturbance is dependent on the size of the earthquake, density of the host material, velocity of the waves and amplitude of disturbance. However, exploring these parameters is beyond the scope of this study and would have wider implications for the host rock stability.

4.7 Conclusion

The timescales associated with homogenous magma compression are important controls on defining the Pe regime of a compressing magma body. We find that for naturally scaled parameters (V_C~$10Km^3$, $Q < 100\text{m}^3/\text{s}$) the gas pressure evolution is well within the equilibrium regime where $Pe \gg 1$. We also find that the effect of viscous resistance is consistent with the findings from the previous chapter where P_η is negligible and the difference between P_g & P_∞ is controlled by P_σ. Extreme values of Q, V_C & N_b which are unlikely for geological constraints are needed to push the Pe regime into disequilibrium. Therefore, empirical calculations for magma compressibility calculated at equilibrium with solubility are feasible. Equation 4.2 is repeated below as a method of calculating magma compressibility by Huppert and Woods (2002):

$$\frac{1}{\beta_m} = \frac{1}{\beta_r} + \frac{1}{\rho}\frac{\partial \rho}{\partial P}$$

Alternatively, when a magma volume change is known (assuming minimal/no elastic response of the magma chamber walls) an implicit expression for P_∞ can be derived based on an individual bubble in the magma, assuming the bubbles are approximated into a lattice and $P_\eta \& P_\sigma$ are omitted due to being negligible:

$$P_\infty \approx P_g = \frac{8.314 n_g(P_g) T}{v_g}, \qquad \text{(Eq. 4.9)}$$

where n_g is calculated based on the solubility concentration:

$$n_g = n_{g0} + \Delta n_g = n_{g0} - \frac{[C(P_g) - C_0]}{100} \frac{1000 \rho_m v_m}{18.015}.$$

The key takeaway from the results of this chapter, is that for reasonable values of natural bubbly magma chamber dimensions, recharge rate and gas compositions, pressurisation of the magma reservoir can be assumes insufficiently fast enough to resorb H_2O at disequilibrium with solubility.

5 Summary and conclusions

Each subsequent iteration of investigations in this thesis has built upon knowledge gained from the previous investigations and have been synthesised in chapter 4 in the context of natural magma reservoirs.

Starting with the first investigation, 2 stripped down a gas-liquid magma reservoir into its simplest components; a cylinder consisting of a gas and liquid layers. This is the simplest way to investigate a gas-solvent liquid system under compression, removing the complexities arising from the geometry of spherical bubbles. While the numerical setup is makes simplifications towards natural setups, it was useful in understanding the fundamental processes occurring when gasses resorb into melt and for quantifying the pressure relationships between volume and pressure of a soluble gas, knowledge that have been useful for the subsequent chapters thereafter. In that chapter, we first identified 3 solutions for calculating gas pressure evolution under a known volumetric compression evolution. Those being 2 analytical end member solutions: 1) no diffusion or resorption end-member, where all the gas molecules remain in the gas phase, representing the maximum pressure evolution of the system; 2) an equilibrium diffusion and resorption end-member, where gas resorption and diffusion through the melt occur instantaneously at equilibrium with the pressure dependent solubility, this represents the minimum pressure evolution of the system. And finally, a numerical solution that accounts for mixed behaviour between the end member solutions. Mixed behaviour arises from the diffusion of H_2O across the melt, the movement of particles across a diffusive medium is predicted by fick's second law. The pressure evolution of a compressing gas-liquid system can be described by a dimensionless Péclet number (Pe) a balance between the relative diffusive and compressive timescales $(\lambda_D \ \& \ \lambda_R)$. Equation 1.10 is repeated below:

$$Pe = \frac{\lambda_R}{\lambda_D} = \frac{R_0 D}{\dot{R} L^2}$$

Three pressure evolution regimes can be identified by the Pe number: $Pe \ll 1$, when diffusion occurs on a much slower timescale than compression, thus pushing the pressure towards the no diffusion end-member regime; $Pe \gg 1$ is the equilibrium regime, where the pressure evolution follows the equilibrium end-member regime, representing the lowest

pressure evolution; and finally $Pe \sim 1$ when the pressure evolution begins to deviate from the equilibrium solution as the timescales are similar. Figure 2.2 has been repeated below (Figure 5.1) to illustrate what the Pe numbers mean in terms of the H_2O concentration profiles over time. A high Pe produces uniform concentration profiles at any given time, thus showing that diffusion and resorption occurs quickly. As the Pe number decreases, H_2O cannot diffuse easily through the melt, thus limiting the resorption of H_2O. The Pe number will prove to be an important concept in the following investigations.

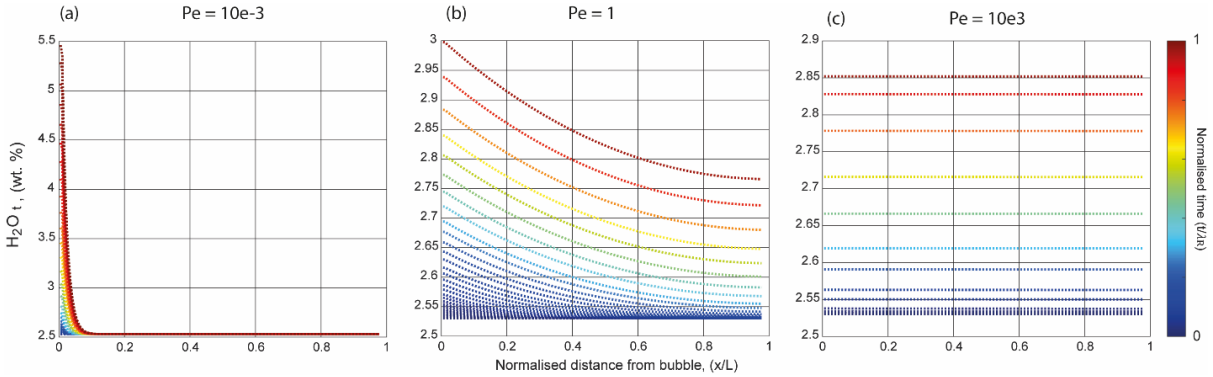

Figure 5.1. ; a repeat of figure 2.2, showing the H_2O concentration profiles during the compression of a soluble gas pocket, for 3 Pe number regimes

In the next chapter (3), more complexity is added to the model to represent a natural bubbly magma a little more. There I introduced spherical coordinates and the 'bubble cell' model by Prousevitchet al., (1993), which models a spherical bubble surrounded by an incompressible melt shell. In terms of gas pressure evolution, calculating a Pe is still applicable and highly useful for determining the pressure evolution regime of the system under compression, the differences from its previous chapter arise from how the melt shell thickens as the bubble shrinks in order to conserve the melt volume, this causes Pe to naturally decay as the bubble shrinks towards zero radius. However, for bubble cells it was found that extremely fast compression timescales (λ_R) were required to push the system into disequilibrium $(Pe \leq 1)$, such fast timescales may be unlikely in nature. Furthermore, I address that the pressure of a magma reservoir is the relative sum of the gas pressure, surface tension acting on the bubble and viscous resistance from the melt, described by the hydrodynamic equation repeated below:

$$P_\infty = P_g - P_\sigma - (-)P_\eta$$

However, we have found that surface tension and viscous resistance $(P_\sigma \ \& \ P_\eta)$ were generally negligible components. P_σ only becomes an important factor when the bubble radius shrinks closer to zero in which case P_σ increases towards infinity, this represents a bubble spontaneously shrinking due to increasingly high surface tensions acting on a tiny bubble. P_η was surprisingly the least important factor, even being several orders of magnitude less than P_σ which in itself is a negligible component. Therefore, one can reasonably assume that the gas pressure P_g is a reasonable reflection of the pressure of a magma P_∞.

Finally in the final chapter (4), everything we have learned in the preceding chapters were synthesised and applied to natural scenarios. There, I setup a new conceptual model for a perfectly rigid bubbly magma reservoir under recharge, in order to isolate the effects of the magma compressibility due to bubbles. The bubbles in the magma reservoir are approximated into a lattice of identical bubble cells, so the pressure evolution of a whole magma reservoir could be calculated by modelling the processes of a single bubble. There we found that for most natural scenarios, the pressure evolution of a bubbly magma reservoir under geological constraints for magma recharge rates are always in the equilibrium pressure regime $(Pe \gg 1)$. There are factors that may push the system close or to disequilibrium (e.g., extremely high magma recharge rates that are unlikely in nature ($Q \gg 100 m^3 s^{-1}$), small magma reservoirs under a high magma recharge rate) but such scenarios are highly unlikely in nature. Therefore, I present an analytical implicit solution of calculating the pressure evolution of a magma reservoir under a known volume recharge rate:

$$P_\infty \approx P_g = \frac{8.314 n_g(P_g) T}{v_g}$$

Where n_g is calculated at solubility with pressure:

$$n_g = \ n_{g0} + \Delta n_g = \ n_{g0} - \frac{[C(P_g) \ - C_0]}{100} \frac{1000 \rho_m v_m}{18.015}$$

There are however many limitations to this method. Firstly, the compressibility due to bubbles is only a single physical property of a magma and so the solution I presented should not be used as a universal solution to calculate the pressure of a magma. This study has neglected the elastic response from the cavity walls and thermal effects as they are beyond the scope of this study. The findings of this study should therefore be used to complement other studies that model the recharge of a magma chamber. The main value of this study is that we can reasonably assume that volatile resorption during the pressurization of a magma reservoir, specifically H_2O, occurs at equilibrium with pressure-dependent solubility of H_2O. Therefore, future studies should focus on this conclusion. This model is only also valid for H_2O, I have not considered the speciation of H_2O, nor other volatile gasses such as CO_2. A separate CO_2 or SO_2 bubble model may be a worthwhile endeavour for future studies as they exsolve at much higher pressures than H_2O, so in deeper magmatic systems, the bubbles may be dominated by CO_2 & SO_2 gasses. The piston-model can solve the pressure evolution of a separate free gas layer accumulated at the top of a magma reservoir (Figure 4.8), where we expect the gas resorption rate to be greatly hindered by the lower specific surface area of the melt-gas interface. We have found that the Pe numbers expected for this scenario to be $\ll 1$, therefore a different numerical model is required to model the pressure evolution for this scenario.

The findings of this study should therefore be used to complement other studies that model the recharge of a magma chamber. The main value of this study is that we can reasonably assume that volatile resorption during the pressurization of a magma reservoir, specifically H_2O occurs at equilibrium with pressure-dependent solubility of H_2O. Therefore, future modelling and theoretical studies should keep these conclusions in mind.

6 Acknowledgements

First and foremost, I would like to thank my parents for partially funding this degree and for allowing me to pursue my passion for learning. Many thanks towards my supervisory team, Prof Ed Llewellin, Dr Fabian Wadsworth and Dr Jason Coumans; I owe this thesis to their guidance, training, discussions and general support, I could not have wished for a better supervisory team. I finally thank VolcCoffee, our volcanology research group for insightful discussions and great company from a community of passionate volcanologists

References

Anderson, A. T. (1995). CO2 and the eruptibility of picrite and komatiite. *LITHOS*. https://doi.org/10.1016/0024-4937(95)90005-5

Blake, S. (1981). Volcanism and the dynamics of open magma chambers Stephen. *Nature*, *289*, 783–785. https://doi.org/10.1017/CBO9781107415324.004

Blower, J. D. Y., Mader, H. M. Y., & Wilson, S. D. R. (2001). *Coupling of viscous and di ¡ usive controls on bubble growth during explosive volcanic eruptions*. *193*, 47–56.

Cashman, K. V., Sparks, R. S. J., & Blundy, J. D. (2017). Vertically extensive and unstable magmatic systems: A unified view of igneous processes. *Science*, *355*(6331). https://doi.org/10.1126/science.aag3055

Christopher, T. E., Blundy, J., Cashman, K., Cole, P., Edmonds, M., Smith, P. J., Sparks, R. S. J., & Stinton, A. (2015). Crustal-scale degassing due to magma system destabilization and magma-gas decoupling at Soufrière Hills Volcano, Montserrat. *Geochemistry, Geophysics, Geosystems*, *16*(9), 2797–2811. https://doi.org/10.1002/2015GC005791

Coumans, J. P., Llewellin, E. W., Wadsworth, F. B., Humphreys, M. C. S., Mathias, S. A., Yelverton, B. M., & Gardner, J. E. (2020). An experimentally validated numerical model for bubble growth in magma. *Journal of Volcanology and Geothermal Research*, *402*, 107002. https://doi.org/10.1016/j.jvolgeores.2020.107002

Degruyter, W., Huber, C., Bachmann, O., Cooper, K. M., & Kent, A. J. R. (2017). Influence of Exsolved Volatiles on Reheating Silicic Magmas by Recharge and Consequences for Eruptive Style at Volcán Quizapu (Chile). *Geochemistry, Geophysics, Geosystems*, *18*(11), 4123–4135. https://doi.org/10.1002/2017GC007219

Degruyter, Wim, Huber, C., Bachmann, O., Cooper, K. M., & Kent, A. J. R. (2016). Magma reservoir response to transient recharge events: The case of Santorini volcano (Greece). *Geology*, *44*(1), 23–26. https://doi.org/10.1130/G37333.1

Delgado, F., Pritchard, M. E., Basualto, D., Lazo, J., Córdova, L., & Lara, L. E. (2016). Rapid reinflation following the 2011–2012 rhyodacite eruption at Cordón Caulle volcano (Southern Andes) imaged by InSAR: Evidence for magma reservoir refill. *Geophysical Research Letters*, *43*(18), 9552–9562. https://doi.org/10.1002/2016GL070066

Edmonds, M., Cashman, K. V., Holness, M., & Jackson, M. (2019a). Architecture and dynamics of magma reservoirs. In *Philosophical Transactions of the Royal Society A: Mathematical, Physical and Engineering Sciences* (Vol. 377, Issue 2139).

https://doi.org/10.1098/rsta.2018.0298

Edmonds, M., Cashman, K. V., Holness, M., & Jackson, M. (2019b). Architecture and dynamics of magma reservoirs. *Philosophical Transactions of the Royal Society A: Mathematical, Physical and Engineering Sciences*, *377*(2139). https://doi.org/10.1098/rsta.2018.0298

Edmonds, M., & Woods, A. W. (2018). Exsolved volatiles in magma reservoirs. *Journal of Volcanology and Geothermal Research*, *368*, 13–30. https://doi.org/10.1016/j.jvolgeores.2018.10.018

Encyclopedia of volcanoes. (2000). In *Encyclopedia of volcanoes.* https://doi.org/10.1029/00eo00168

Farrell, J., Smith, B. R., Husen, S., & Diehl, T. (2014). beyond the Yellowstone caldera. *AGU Publications, Geophysical Research Letters*, 3068–3073. https://doi.org/10.1002/2014GL059588.Received

Gerya, T. (2019). Density and gravity. In *Introduction to Numerical Geodynamic Modelling* (2nd ed., pp. 26–37). Cambridge University Press. https://doi.org/10.1017/9781316534243.003

Giordano, D., Russell, J. K., & Dingwell, D. B. (2008). Viscosity of magmatic liquids: A model. *Earth and Planetary Science Letters*, *271*(1–4), 123–134. https://doi.org/10.1016/j.epsl.2008.03.038

Gudmundsson, A. (1988). Effect of tensile stress concentration around magma chambers on intrusion and eruption. *Journal of Volcanology and Geothermal Research*, 35(1–2), 255–264. https://doi.org/10.1016/0377-0273(88)90015-7

Gudmundsson, A., 2012. Magma chambers: Formation, local stresses, excess pressures, and compartments. *Journal of Volcanology and Geothermal Research*, *237*, pp.19-41.

Hess, K. U., & Dingwell, D. B. (1996). Viscosities of hydrous leucogranitic melts: a non-Arrhenian model. *American Mineralogist*, *81*(9–10), 1297–1300. https://doi.org/10.2138/am-1996-9-1031

Huppert, H. E., & Woods, A. W. (2002). The role of volatiles in magma chamber dynamics. *Nature*, *420*(6915), 493–495. https://doi.org/10.1038/nature01211

Kilbride, B. M. C., Edmonds, M., & Biggs, J. (2016). Observing eruptions of gas-rich compressible magmas from space. *Nature Communications*, *7*, 1–8. https://doi.org/10.1038/ncomms13744

Le Mével, H., Gregg, P. M., & Feigl, K. L. (2016). Magma injection into a long-lived reservoir to explain geodetically measured uplift: Application to the 2007–2014 unrest episode at Laguna del Maule volcanic field, Chile. *Journal of Geophysical Research: Solid Earth*, *121*(8), 6092–6108. https://doi.org/10.1002/2016JB013066

Lesher, C. E., & Spera, F. J. (2015). Thermodynamic and Transport Properties of Silicate Melts and Magma. In *The Encyclopedia of Volcanoes*. https://doi.org/10.1016/b978-0-12-385938-9.00005-5

Liu, Y., Zhang, Y., & Behrens, H. (2005). Solubility of H 2 O in rhyolitic melts at low pressures and a new empirical model for mixed H 2 O-CO 2 solubility in rhyolitic melts. *Journal of Volcanology and Geothermal Research*, *143*(1–3), 219–235. https://doi.org/10.1016/j.jvolgeores.2004.09.019

Lyakhovsky, V., Hurwitz, S., & Navon, O. (1996). Bubble growth in rhyolitic melts: Experimental and numerical investigation. *Bulletin of Volcanology*, *58*(1), 19–32. https://doi.org/10.1007/s004450050122

Marsh, B. D. (1981). On the crystallinity, probability of occurrence, and rheology of lava and magma. *Contributions to Mineralogy and Petrology*, *78*(1), 85–98. https://doi.org/10.1007/BF00371146

McBirney, A. R., & Murase, T. (1970). Factors governing the formation of pyroclastic rocks. *Bulletin Volcanologique*. https://doi.org/10.1007/BF02596762

Mogi, K. (1958). Relations between the eruptions of various volcanoes and the deformations of the ground surfaces around them. In *Bulletin of the Earthquake Research Institute*. https://doi.org/10.1016/j.epsl.2004.04.016

Newman, A. V., Stiros, S., Feng, L., Psimoulis, P., Moschas, F., Saltogianni, V., Jiang, Y., Papazachos, C., Panagiotopoulos, D., Karagianni, E., & Vamvakaris, D. (2012). Recent geodetic unrest at Santorini Caldera, Greece. *Geophysical Research Letters*, *39*(6), 1–5. https://doi.org/10.1029/2012GL051286

Parmigiani, A., Faroughi, S., Huber, C., Bachmann, O., & Su, Y. (2016). Bubble accumulation and its role in the evolution of magma reservoirs in the upper crust. *Nature*, *532*(7600), 492–495. https://doi.org/10.1038/nature17401

Petford, N., Cruden, A. R., McCaffrey, K. J. W., & Vigneresse, J. L. (2000). Granite magma formation, transport and emplacement in the Earth's crust. *Nature*, *408*(6813), 669–673. https://doi.org/10.1038/35047000

Popa, R. G., Bachmann, O., Ellis, B. S., Degruyter, W., Tollan, P., & Kyriakopoulos, K. (2019). A connection between magma chamber processes and eruptive styles revealed at Nisyros-Yali volcano (Greece). *Journal of Volcanology and Geothermal Research*, *387*. https://doi.org/10.1016/j.jvolgeores.2019.106666

Prousevitch, A. A., Sahagian, D. L., & Anderson, A. T. (1993a). Dynamics of diffusive bubble growth in magmas: isothermal case. *Journal of Geophysical Research*. https://doi.org/10.1029/93jb02027

Prousevitch, A. A., Sahagian, D. L., & Anderson, A. T. (1993b). Dynamics of diffusive bubble growth in magmas: isothermal case. *Journal of Geophysical Research*, *98*(B12). https://doi.org/10.1029/93jb02027

Proussevitch, A. A., & Sahagian, D. L. (1998). Dynamics and energetics of bubble growth in magmas: Analytical formulation and numerical modeling. *Journal of Geophysical Research: Solid Earth*, *103*(B8), 18223–18251. https://doi.org/10.1029/98jb00906

Rivalta, E., & Segall, P. (2008). Magma compressibility and the missing source for some dike intrusions. *Geophysical Research Letters*, *35*(4), 1–5. https://doi.org/10.1029/2007GL032521

Roscoe, R. (1952). The viscosity of suspensions of rigid spheres. *British Journal of Applied Physics*. https://doi.org/10.1088/0508-3443/3/8/306

Segall, P. (2019). Magma chambers: What we can, and cannot, learn from volcano geodesy. *Philosophical Transactions of the Royal Society A: Mathematical, Physical and Engineering Sciences*, *377*(2139). https://doi.org/10.1098/rsta.2018.0158

Shampine, L. F., & Reichelt, M. W. (1997). The MATLAB ode suite. *SIAM Journal of Scientific Computing*. https://doi.org/10.1137/S1064827594276424

Shaw, H. R. (1972). Viscosities of magmatic silicate liquids; an empirical method of prediction. *American Journal of Science*. https://doi.org/10.2475/ajs.272.9.870

Sparks, R. S. J. (1978). The dynamics of bubble formation and growth in magmas: A review and analysis. *Journal of Volcanology and Geothermal Research*, *3*(1–2), 1–37. https://doi.org/10.1016/0377-0273(78)90002-1

Tuffen, H., & Castro, J. M. (2009). The emplacement of an obsidian dyke through thin ice: Hrafntinnuhryggur, Krafla Iceland. *Journal of Volcanology and Geothermal Research*, *185*(4), 352–366. https://doi.org/10.1016/j.jvolgeores.2008.10.021

Verhoogen, J. (1951). Mechanics of ash formation. *American Journal of Science*.

https://doi.org/10.2475/ajs.249.10.729

Wallace, P. J., Plank, T., Edmonds, M., & Hauri, E. H. (2015). Chapter 7 – Volatiles in Magmas. In *The Encyclopedia of Volcanoes*.

Zhang, Y., & Ni, H. (2010). Diffusion of H, C, and O components in silicate melts. *Reviews in Mineralogy and Geochemistry*, *72*(September 2016), 171–225. https://doi.org/10.2138/rmg.2010.72.5

Appendix A – Model flowcharts

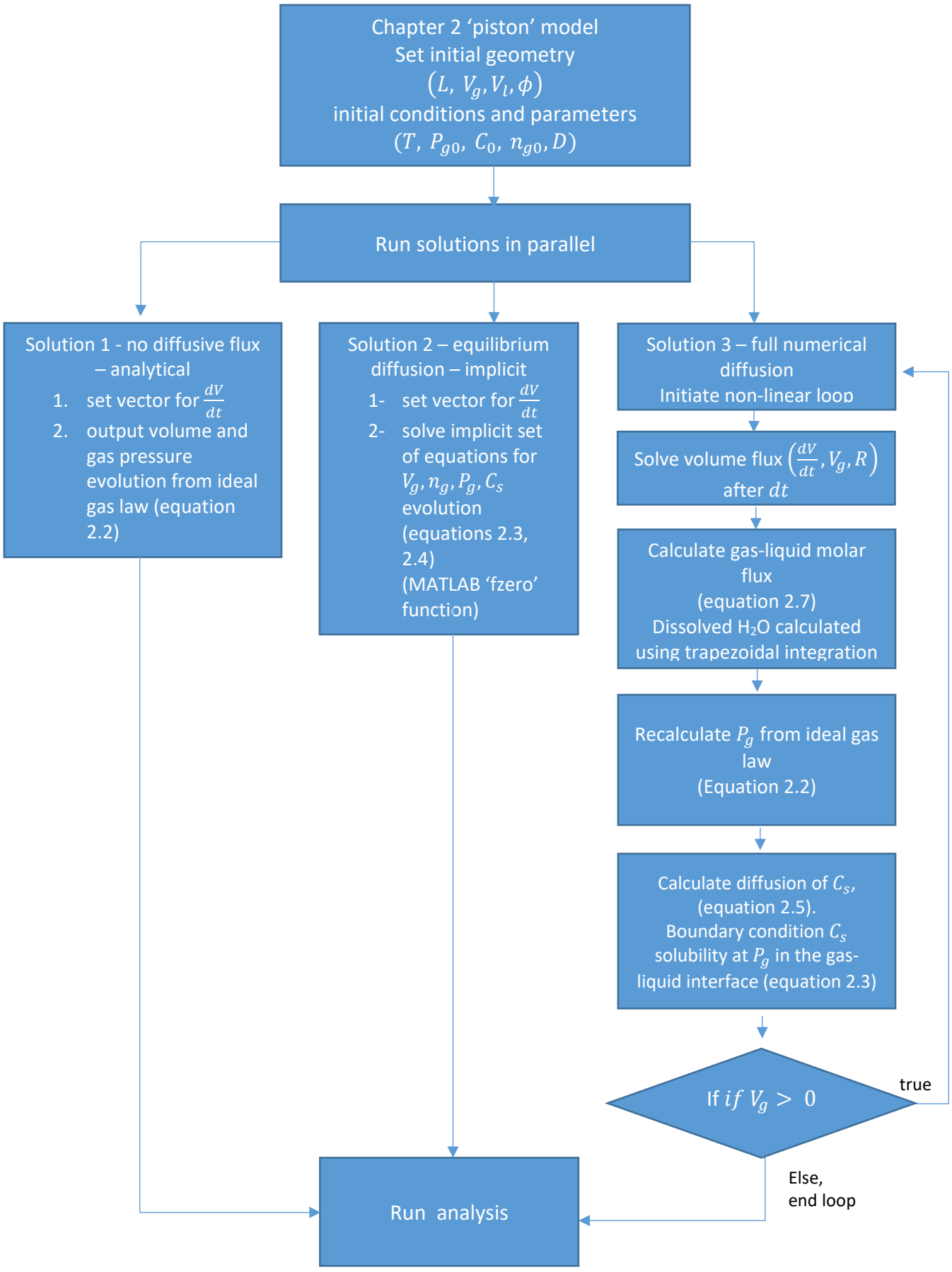

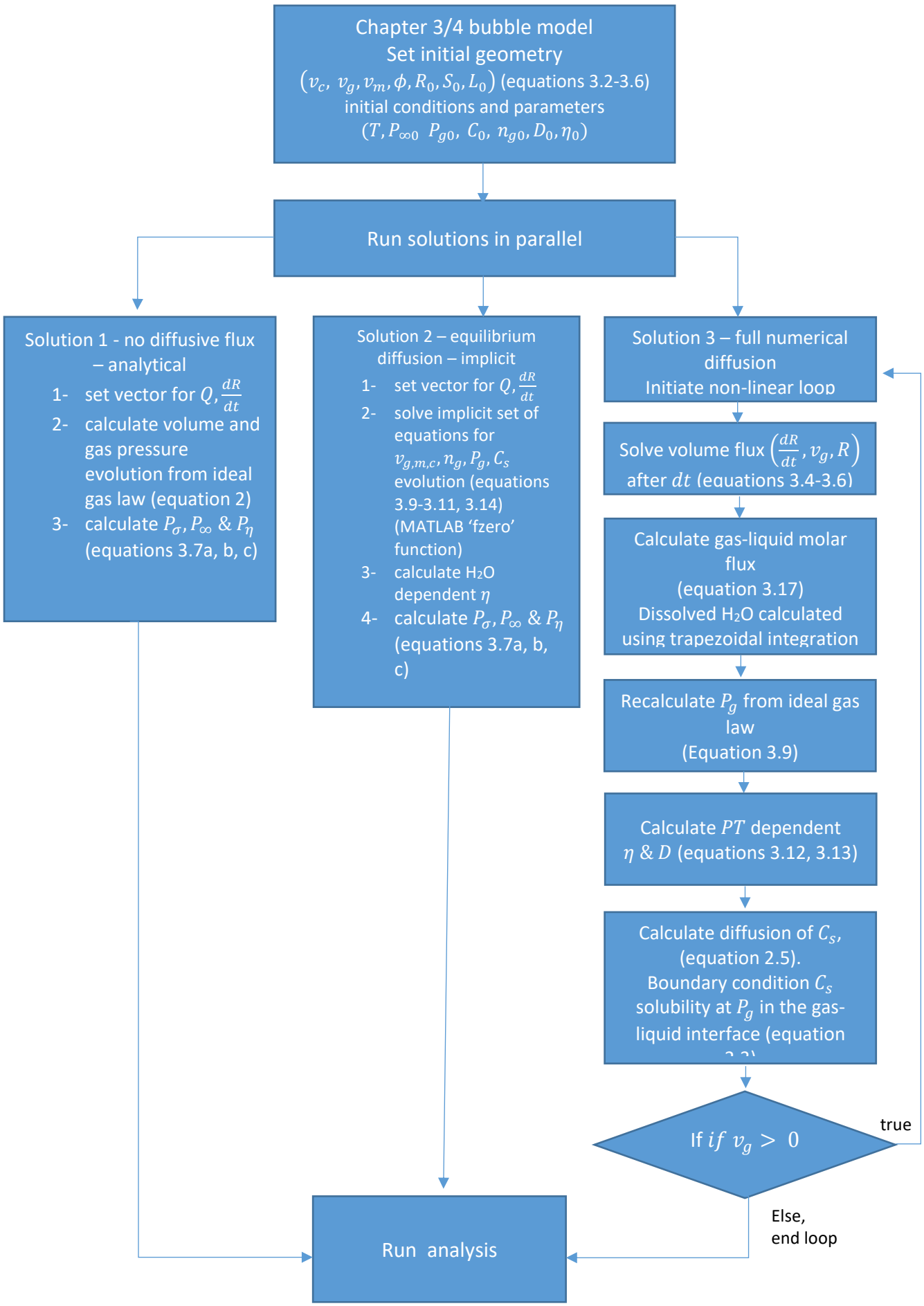
Chapter 3/4 bubble model
Set initial geometry
$(v_c, v_g, v_m, \phi, R_0, S_0, L_0)$ (equations 3.2-3.6)
initial conditions and parameters
$(T, P_{\infty 0}\ P_{g0}, C_0, n_{g0}, D_0, \eta_0)$
Run solutions in parallel
Solution 1 - no diffusive flux – analytical
1- set vector for $Q, \frac{dR}{dt}$
2- calculate volume and gas pressure evolution from ideal gas law (equation 2)
3- calculate P_σ, P_∞ & P_η (equations 3.7a, b, c)
Solution 2 – equilibrium diffusion – implicit
1- set vector for $Q, \frac{dR}{dt}$
2- solve implicit set of equations for $v_{g,m,c}, n_g, P_g, C_s$ evolution (equations 3.9-3.11, 3.14) (MATLAB 'fzero' function)
3- calculate H_2O dependent η
4- calculate P_σ, P_∞ & P_η (equations 3.7a, b, c)
Solution 3 – full numerical diffusion
Initiate non-linear loop
Solve volume flux $\left(\frac{dR}{dt}, v_g, R\right)$ after dt (equations 3.4-3.6)
Calculate gas-liquid molar flux (equation 3.17)
Dissolved H_2O calculated using trapezoidal integration
Recalculate P_g from ideal gas law (Equation 3.9)
Calculate PT dependent η & D (equations 3.12, 3.13)
Calculate diffusion of C_s, (equation 2.5).
Boundary condition C_s solubility at P_g in the gas-liquid interface (equation
If $if\ v_g > 0$
true
Else,
end loop
Run analysis

Appendix B – magma compositions used to calculate viscosity and diffusivity

	SiO2	TiO2	Al2O3	FeO+Fe2O3	MnO	MgO	CaO	Na2O	K2O	P2O
Krafla Tuffen and Castro (2009)	75.17	0.22	12.02	3.13	0.11	0.09	1.66	4.58	2.88	0
Metaluminous rhyolite Encyclopedia of volcanoes (2000)	67.98	0.45	14.49	3.84	0.08	1.75	3.78	3.78	3.05	0.11